

# Superconductivity by Hidden Spin Fluctuations in Electron-Doped Iron Selenide

J.P. Rodriguez<sup>1</sup>

<sup>1</sup>*Department of Physics and Astronomy,  
California State University, Los Angeles, California 90032*

## Abstract

Berg, Metlitski and Sachdev, *Science* **338**, 1606 (2012), have shown that the exchange of hidden spin fluctuations by conduction electrons with two orbitals can result in high-temperature superconductivity in copper-oxide materials. We introduce a similar model for high-temperature iron-selenide superconductors that are electron doped. Conduction electrons carry the minimal  $3d_{xz}$  and  $3d_{yz}$  iron-atom orbitals. Low-energy hidden spin fluctuations at the checkerboard wavevector  $Q_{AF}$  result from nested Fermi surfaces at the center and at the corner of the unfolded (one-iron) Brillouin zone. Magnetic frustration from super-exchange interactions via the selenium atoms stabilize hidden spin fluctuations at  $Q_{AF}$  versus true spin fluctuations. At half filling, Eliashberg theory based purely on the exchange of hidden spin fluctuations reveals a Lifshitz transition to electron/hole Fermi surface pockets at the corner of the folded (two-iron) Brillouin zone, but with vanishing spectral weights. The underlying hidden spin-density wave groundstate is therefore a Mott insulator. Upon electron doping, Eliashberg theory finds that the spectral weights of the hole Fermi surface pockets remain vanishingly small, while the spectral weights of the larger electron Fermi surface pockets become appreciable. This prediction is therefore consistent with the observation of electron Fermi surface pockets alone in electron-doped iron selenide by angle-resolved photoemission spectroscopy (ARPES). Eliashberg theory also finds an instability to  $S^{+-}$  superconductivity at electron doping, with isotropic Cooper pairs that alternate in sign between the visible electron Fermi surface pockets and the faint hole Fermi surface pockets. Comparison with the isotropic energy gaps observed in electron-doped iron selenide by ARPES and by scanning tunneling microscopy (STM) is made.

## I. INTRODUCTION

Electron-doped iron selenides are perhaps the most interesting class of materials inside the family of iron-based superconductors<sup>1-4</sup>. By contrast with bulk FeSe, which is a low-temperature superconductor, a monolayer of FeSe on a doped strontium-titanate substrate becomes a high-temperature superconductor<sup>5</sup>, with a critical temperature in the range 40-50 K<sup>6,7</sup>, and possibly higher<sup>8</sup>. Angle-resolved photoemission spectroscopy (ARPES) reveals that the substrate injects electrons into the FeSe monolayer that bury the hole bands at the center of the Brillouin zone below the Fermi level<sup>9</sup>. ARPES also reveals an energy gap at the remaining electron-type Fermi surface pockets at the corner of the folded (two-iron) Brillouin zone<sup>10,11</sup>. It agrees with the energy gap found by scanning tunneling microscopy (STM)<sup>5,12</sup>. On the other hand, transport studies find perfect conductivity below the critical temperature where the gap opens in ARPES and in STM<sup>6</sup>. These probes provide compelling evidence for a superconducting state at high temperature. Electron doping of FeSe layers can also be achieved by other means, such as by alkali-atom intercalation<sup>1-4</sup>, by organic-molecule intercalation<sup>13-15</sup>, by dosing with alkali atoms<sup>16,17</sup>, and by the application of a gate voltage<sup>18,19</sup>. Again, the result is the same Lifshitz transition of the Fermi surface topology, where the hole bands are buried below the Fermi level, accompanied by high-temperature superconductivity.

The coincidence of high-temperature superconductivity with the absence of Fermi surface nesting in electron-doped FeSe is puzzling. High-temperature superconductivity in iron-pnictide materials occurs only when the Fermi surfaces exhibit partial nesting, for example. In particular, the end-member compound  $\text{KFe}_2\text{As}_2$  of the series of iron-pnictide compounds<sup>20</sup>  $(\text{Ba}_{1-x}\text{K}_x)\text{Fe}_2\text{As}_2$  shows only hole-type Fermi surface pockets at the center of the Brillouin zone<sup>21</sup>. It, however, is a low-temperature superconductor with  $T_c \cong 3$  K. Early theoretical responses to the puzzle posed by electron-doped iron selenide proposed a nodeless  $D$ -wave superconducting state<sup>22,23</sup>, with a full gap over each electron pocket that alternates in sign between them. In the case of bulk electron-doped iron-selenide materials, it was argued that strong dispersion of the energy bands along the  $c$  axis results in inner and outer electron Fermi surface pockets at the corner of the two-iron Brillouin zone because of hybridization due to the two inequivalent iron sites, and that true  $D$ -wave nodes appear as a result<sup>24</sup>. In the case of an isolated layer of FeSe, the two electron Fermi surface pockets at the corner of the

two-iron Brillouin zone cross, but do not hybridize, because of glide-reflection symmetry<sup>25</sup>. Inner and outer electron Fermi surface pockets due to hybridization are predicted when strong enough spin-orbit coupling is included, however, and true  $D$ -wave nodes are again predicted<sup>26-28</sup>. These considerations led to the proposal of the anti-bonding  $S^{+-}$  state. It is an isotropic Cooper pair state that alternates in sign between the inner and the outer electron Fermi surfaces at the corner of the folded (two-iron) Brillouin zone<sup>24,29</sup>. ARPES finds no sign of nodes in the gap and no sign of hybridization on the electron Fermi surface pockets<sup>10,11</sup>, however. Further, STM and the dependence of the specific heat and of nuclear magnetic resonance (NMR) on temperature are consistent with a gap over the entire Fermi surface<sup>3-5</sup>. These measurements could then rule out the nodeless  $D$ -wave state and the anti-bonding  $S^{+-}$  state in high- $T_c$  iron-selenide superconductors.

Below, we will show that a spin-fermion model over the square lattice that is similar to that introduced by Berg, Metlitski and Sachdev in the context of copper-oxide high-temperature superconductors<sup>30</sup> harbors an alternative solution to the puzzling isotropic gap shown by electron-doped iron selenide. The non-interacting electrons are in the principal  $3d_{xz}$  and  $3d_{yz}$  iron orbitals, and they form a semi-metallic Fermi surface that is nested by the checkerboard wavevector  $\mathbf{Q}_{\text{AF}} = (\pi/a, \pi/a)$ . The latter can result in hidden magnetic order when magnetic frustration is present<sup>31</sup>. Such hidden antiferromagnetism is characterized by the most symmetric of three possible order parameters for a hidden spin density wave (hSDW):

$$\frac{1}{2\mathcal{N}} \sum_i e^{i\mathbf{Q}_{\text{AF}} \cdot \mathbf{r}_i} \sum_{s=\uparrow, \downarrow} (\text{sgn } s) i \langle c_{i,d_{xz},s}^\dagger c_{i,d_{yz},s} - c_{i,d_{yz},s}^\dagger c_{i,d_{xz},s} \rangle,$$

where  $\mathcal{N}$  is the number of site-orbitals. It is isotropic with respect to rotations of the orbitals about the  $z$  axis, and it therefore does not couple to nematicity. (Cf. refs.<sup>32,33</sup>.) Based on the interaction of such fermions with the corresponding hidden spin fluctuations, an Eliashberg theory for  $S$ -wave pairing over the two bands of electrons is developed. Hopping matrix elements are chosen so that perfect nesting exists at half filling<sup>31</sup>. As the interaction grows strong, we find (i) a Lifshitz transition to electron-type and hole-type Fermi surface pockets at the corner of the folded (two-iron) Brillouin zone. The new Fermi surfaces remain perfectly nested by  $\mathbf{Q}_{\text{AF}}$ , but their spectral weights are vanishingly small due to strong wavefunction renormalization. Upon electron doping, the hole Fermi surfaces remain faint, while the electron Fermi surfaces become visible because of only moderate wavefunction renor-

malization. This prediction agrees with previous calculations based on the corresponding local-moment model<sup>34</sup>. The Eliashberg theory also reveals (*ii*) an instability at the renormalized Fermi surface to  $S^{+-}$  pairing that alternates in sign between the visible electron-type Fermi surfaces and the faint hole-type Fermi surfaces. We shall now provide details of how such hidden  $S^{+-}$  superconductivity emerges from the two-band Eliashberg theory.

## II. BARE NESTED FERMI SURFACES AND HIDDEN SPIN FLUCTUATIONS

The conditions for perfect nesting of the Fermi surfaces in two-orbital hopping Hamiltonians for iron selenide will be determined in what follows<sup>31</sup>. Also, the space of hSWD states generated by rotations of the two isospin degrees of freedom, the  $d+$  and  $d-$  orbitals, will also be discussed.

### A. Electron Hopping

The electronic kinetic energy is governed by the hopping Hamiltonian

$$H_{\text{hop}} = - \sum_{\langle i,j \rangle} (t_1^{\alpha,\beta} c_{i,\alpha,s}^\dagger c_{j,\beta,s} + \text{h.c.}) - \sum_{\langle\langle i,j \rangle\rangle} (t_2^{\alpha,\beta} c_{i,\alpha,s}^\dagger c_{j,\beta,s} + \text{h.c.}), \quad (1)$$

where the repeated indices  $\alpha$  and  $\beta$  are summed over the iron  $3d$  orbitals, where the repeated index  $s$  is summed over electron spin, and where  $\langle i, j \rangle$  and  $\langle\langle i, j \rangle\rangle$  represent nearest neighbor (1) and next-nearest neighbor (2) links on the square lattice of iron atoms. Above,  $c_{i,\alpha,s}$  and  $c_{i,\alpha,s}^\dagger$  denote annihilation and creation operators for an electron of spin  $s$  in orbital  $\alpha$  at site  $i$ . We keep only the  $3d_{xz}$  and  $3d_{yz}$  orbitals of the iron atoms, which are the principal ones in iron selenide. In particular, let us work in the isotropic basis of orbitals  $d- = (d_{xz} - id_{yz})/\sqrt{2}$  and  $d+ = (d_{xz} + id_{yz})/\sqrt{2}$ . The reflection symmetries shown by a single layer of iron selenide imply that the above intra-orbital and inter-orbital hopping matrix elements show  $s$ -wave and  $d$ -wave symmetry, respectively<sup>25,35,36</sup>. In particular, nearest neighbor hopping matrix elements satisfy

$$\begin{aligned} t_1^{\pm\pm}(\hat{\mathbf{x}}) &= t_1^\parallel = t_1^{\pm\pm}(\hat{\mathbf{y}}) \\ t_1^{\pm\mp}(\hat{\mathbf{x}}) &= t_1^\perp = -t_1^{\pm\mp}(\hat{\mathbf{y}}), \end{aligned} \quad (2)$$

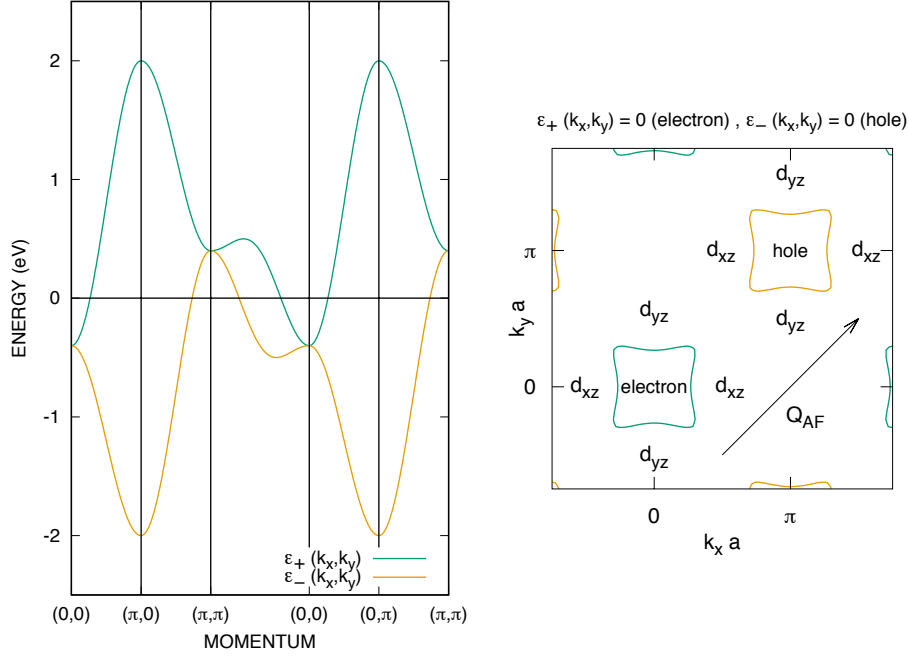


FIG. 1: Band structure with perfectly nested Fermi surfaces at half filling:  $\varepsilon_+(\mathbf{k}) = 0$  and  $\varepsilon_-(\mathbf{k}) = 0$ , with hopping matrix elements  $t_1^\parallel = 100$  meV,  $t_1^\perp = 500$  meV,  $t_2^\parallel = 0$ , and  $t_2^\perp/i = 100$  meV.

where  $t_1^\parallel$  and  $t_1^\perp$  are real, while next-nearest neighbor hopping matrix elements satisfy

$$\begin{aligned}
 t_2^{\pm\pm}(\hat{\mathbf{x}} + \hat{\mathbf{y}}) &= t_2^\parallel = t_2^{\pm\pm}(\hat{\mathbf{y}} - \hat{\mathbf{x}}) \\
 t_2^{\pm\mp}(\hat{\mathbf{x}} + \hat{\mathbf{y}}) &= \pm t_2^\perp = -t_2^{\pm\mp}(\hat{\mathbf{y}} - \hat{\mathbf{x}}),
 \end{aligned}
 \tag{3}$$

where  $t_2^\parallel$  is real, and where  $t_2^\perp$  is pure imaginary.

The above hopping Hamiltonian  $H_{\text{hop}}$  then has intra-orbital and inter-orbital matrix elements

$$\varepsilon_\parallel(\mathbf{k}) = -2t_1^\parallel(\cos k_x a + \cos k_y a) - 2t_2^\parallel(\cos k_+ a + \cos k_- a)
 \tag{4a}$$

$$\varepsilon_\perp(\mathbf{k}) = -2t_1^\perp(\cos k_x a - \cos k_y a) - 2t_2^\perp(\cos k_+ a - \cos k_- a)
 \tag{4b}$$

with  $k_\pm = k_x \pm k_y$ . It is easily diagonalized by plane waves of  $d_{x(\delta)z}$  and  $i d_{y(\delta)z}$  orbitals that

are rotated with respect to the principal axes by an angle  $\delta(\mathbf{k})$ :

$$\begin{aligned} |\mathbf{k}, d_{x(\delta)z}\rangle &= \mathcal{N}^{-1/2} \sum_i e^{i\mathbf{k}\cdot\mathbf{r}_i} [e^{i\delta(\mathbf{k})}|i, d+\rangle + e^{-i\delta(\mathbf{k})}|i, d-\rangle], \\ i|\mathbf{k}, d_{y(\delta)z}\rangle &= \mathcal{N}^{-1/2} \sum_i e^{i\mathbf{k}\cdot\mathbf{r}_i} [e^{i\delta(\mathbf{k})}|i, d+\rangle - e^{-i\delta(\mathbf{k})}|i, d-\rangle], \end{aligned} \quad (5)$$

where  $\mathcal{N} = 2N_{\text{Fe}}$  is the number of iron site-orbitals. The phase shift  $\delta(\mathbf{k})$  is set by  $\varepsilon_{\perp}(\mathbf{k}) = |\varepsilon_{\perp}(\mathbf{k})|e^{i2\delta(\mathbf{k})}$ . Specifically,

$$\cos 2\delta(\mathbf{k}) = \frac{-t_1^{\perp}(\cos k_x a - \cos k_y a)}{\sqrt{t_1^{\perp 2}(\cos k_x a - \cos k_y a)^2 + |2t_2^{\perp}|^2(\sin k_x a)^2(\sin k_y a)^2}}, \quad (6a)$$

$$\sin 2\delta(\mathbf{k}) = \frac{2(t_2^{\perp}/i)(\sin k_x a)(\sin k_y a)}{\sqrt{t_1^{\perp 2}(\cos k_x a - \cos k_y a)^2 + |2t_2^{\perp}|^2(\sin k_x a)^2(\sin k_y a)^2}}. \quad (6b)$$

The phase shift is notably singular at  $\mathbf{k} = 0$  and  $\mathbf{Q}_{\text{AF}} = (\pi/a, \pi/a)$ , where the matrix element  $\varepsilon_{\perp}(\mathbf{k})$  vanishes. The energy eigenvalues of the bonding (+) and anti-bonding (-) plane waves (5) are respectively given by  $\varepsilon_+(\mathbf{k}) = \varepsilon_{\parallel}(\mathbf{k}) + |\varepsilon_{\perp}(\mathbf{k})|$  and  $\varepsilon_-(\mathbf{k}) = \varepsilon_{\parallel}(\mathbf{k}) - |\varepsilon_{\perp}(\mathbf{k})|$ .

Henceforth, we shall turn off next-nearest neighbor intra-orbital hopping:  $t_2^{\parallel} = 0$ . Notice that the above energy bands now satisfy the perfect nesting condition

$$\varepsilon_{\pm}(\mathbf{k} + \mathbf{Q}_{\text{AF}}) = -\varepsilon_{\mp}(\mathbf{k}), \quad (7)$$

where  $\mathbf{Q}_{\text{AF}} = (\pi/a, \pi/a)$  is the checkerboard wavevector on the square lattice of iron atoms. The Fermi level at half filling therefore lies at  $\epsilon_{\text{F}} = 0$ . Figure 1 displays perfectly nested electron-type and hole-type Fermi surfaces for hopping parameters  $t_1^{\parallel} = 100$  meV,  $t_1^{\perp} = 500$  meV,  $t_2^{\parallel} = 0$  and  $t_2^{\perp}/i = 100$  meV. Figure 2 shows the density of states of the bonding (+) band.

## B. Hidden Magnetic Order

The true electronic spin at a site  $i$  is measured by the operator  $\mathbf{S}_i = (\hbar/2) \sum_{s,s'} \sum_{\alpha} c_{i,\alpha,s}^{\dagger} \boldsymbol{\sigma}_{s,s'} c_{i,\alpha,s'}$ , where  $\boldsymbol{\sigma}$  are the Pauli matrices. Hidden spin excitations must then be orthogonal to true spin excitations. In the present case, we keep only the principal  $d-$  and  $d+$  orbitals,  $\alpha$ . Hidden spin excitations then corresponds to ‘‘pion’’ excitations of the latter isospin degrees of freedom. Table I lists these spin excitations explicitly, which have isospin  $I = 1$ . Notice that hidden spin excitations generated by the  $(\pi^0)$  operator

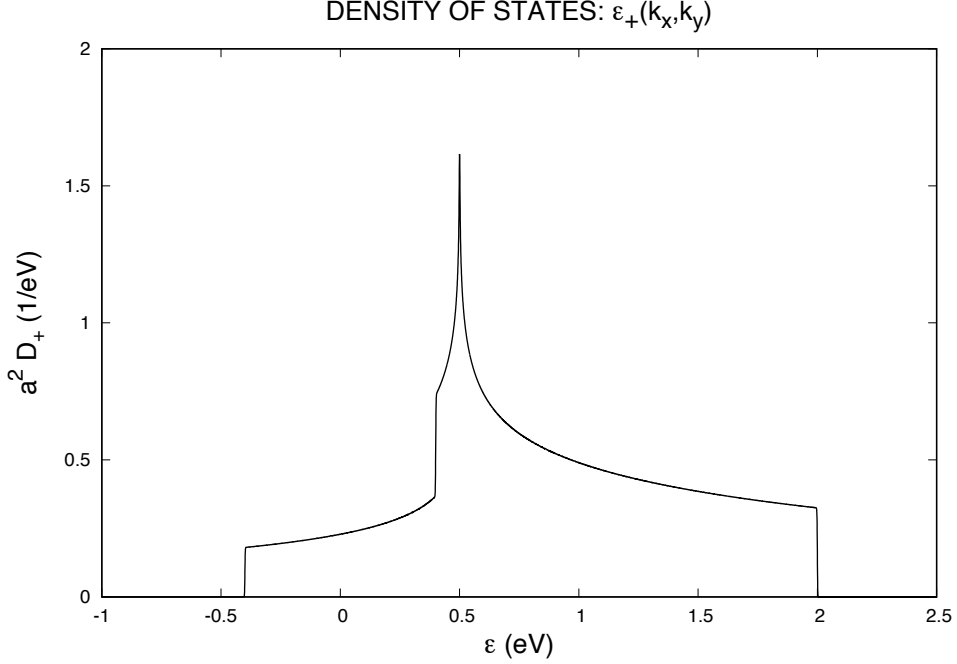


FIG. 2: Density of states of the bonding band evaluated numerically at hopping parameters that are listed in the caption to Fig. 1:  $a^2 D_+(\varepsilon) = N_{\text{Fe}}^{-1} \sum_{\mathbf{k}} \delta[\varepsilon - \varepsilon_+(\mathbf{k})]$ . The unfolded (one-iron) Brillouin zone is divided into a  $10,000 \times 10,000$  grid, while the  $\delta$ -function is approximated by  $(4k_B T_0)^{-1} \text{sech}^2(\varepsilon/2k_B T_0)$ . Here,  $k_B T_0$  is 3 parts in 10,000 of the bandwidth.

$\mathbf{S}_i(\pi) = (\hbar/2) \sum_{s,s'} (c_{i,d-,s}^\dagger \boldsymbol{\sigma}_{s,s'} c_{i,d-,s'} - c_{i,d+,s}^\dagger \boldsymbol{\sigma}_{s,s'} c_{i,d+,s'})$  are the most symmetric ones, showing isotropy about the orbital  $z$  axis. This becomes explicit after writing  $\mathbf{S}_i(\pi)$  in terms of  $d_{xz}$  and  $d_{yz}$  orbitals, which appears in the row corresponding to the isospin quantization axis  $I_3$  in Table II.

The perfect nesting of the electron-type and hole-type Fermi surfaces that exists at half filling and  $t_2^\parallel = 0$ , and that is displayed by Fig. 1, implies an instability to a spin-density wave at the wavevector corresponding to Néel antiferromagnetic order,  $\mathbf{Q}_{\text{AF}} = (\pi/a, \pi/a)$ . An extended Hubbard model that adds on-site Coulomb repulsion to the electron hopping Hamiltonian (1), and that also includes magnetic frustration due to super-exchange via the selenium atoms, was recently introduced by the author and Melendrez<sup>31</sup>. (See Appendix A.) The Heisenberg exchange interactions that express the latter notably show  $SU(2)$  rotation

symmetry among the isospins  $d+$  and  $d-$ . A standard mean-field analysis finds hidden spin-density wave (hSDW) order at wavevector  $\mathbf{Q}_{\text{AF}}$ , with opposing magnetic moments per  $d+$  and  $d-$  orbital that also alternate in sign in a checkerboard fashion over the square lattice of iron atoms. The hSDW is stable at moderate to strong magnetic frustration, in which case the conventional spin-density wave (SDW) at wavevector  $\mathbf{Q}_{\text{AF}}$ , with magnetic moments that are aligned per  $d+$  and  $d-$  orbitals, is suppressed. Two other types of hidden magnetic moments are listed in the last two rows of Table I. The first two rows of Table II,  $I_1$  and  $I_2$ , make up the same subspace of hidden magnetic moments, but in terms of  $d_{xz}$  and  $d_{yz}$  orbitals instead. Such hidden magnetic moments have non-zero isospin quantum number  $I_3$ . The corresponding hSDW states should therefore lie at higher energy compared to the former hSDW state, which is made up of hidden magnetic moments that are orbitally isotropic about the  $z$  axis<sup>31</sup> ( $I_3 = 0$ ).

The long-range hidden Néel order shown by the hSDW state implies low-energy spin-wave excitations that collapse to zero energy at the ordering wavevector  $\mathbf{Q}_{\text{AF}}$ . These hidden spinwaves emerge from the dynamics between the bulk spin,  $\mathbf{S} = \sum_i (\mathbf{S}_{i,d-} + \mathbf{S}_{i,d+})$ , and the hidden ordered magnetic moment<sup>31</sup>,  $\mathbf{m}(\pi) = N_{\text{Fe}}^{-1} \sum_i e^{i\mathbf{Q}_{\text{AF}} \cdot \mathbf{r}_i} (\mathbf{S}_{i,d-} - \mathbf{S}_{i,d+})$ . It is yet another example of antiferromagnetic dynamics first discovered by Anderson<sup>37-39</sup>. The previous are conjugate dynamical variables that satisfy the commutation relations  $[S_i, m_j(\pi)] = i\hbar \epsilon_{i,j,k} m_k(\pi)$ . At the long-wavelength limit, they lead to dynamics governed by the non-linear  $\sigma$ -model, which is a functional of the unit vector field  $\mathbf{n} = \mathbf{m}(\pi)/|\mathbf{m}(\pi)|$ . Its Lagrangian is given by  $L = \int d^2r \frac{1}{2} (\chi_{\perp} |\dot{\mathbf{n}}|^2 - \rho_s |\nabla \mathbf{n}|^2)$ , where  $\chi_{\perp}$  is the spin susceptibility of the hSDW for external magnetic field applied perpendicular to the hidden ordered magnetic moment,  $\mathbf{m}(\pi)$ , and where  $\rho_s$  is the spin rigidity of the hSDW.

Now assume that the hSDW spontaneously breaks symmetry along the  $z$  axis. The dynamical propagator for hidden spinwaves can then be defined as  $iD(\mathbf{q}, \omega) = \langle \frac{1}{\sqrt{2}} m^+(\pi) \frac{1}{\sqrt{2}} m^-(\pi) \rangle_{\mathbf{q}, \omega}$ , where  $m^{\pm}(\pi) = m_x(\pi) \pm i m_y(\pi)$ . It can be read off directly from the Lagrangian of the non-linear  $\sigma$ -model, yielding the universal form

$$D(\mathbf{q}, \omega) = \frac{(2s_1)^2}{\chi_{\perp}} [\omega^2 - \omega_b^2(\mathbf{q})]^{-1} \quad (8)$$

at long wavelength and low frequency<sup>38,39</sup>. Here,  $2s_1\hbar$  is the magnitude of the hidden ordered magnetic moment,  $\mathbf{m}(\pi)$ , at an iron site. Above, the poles in frequency disperse as

$$\omega_b(\mathbf{q}) = (c_b^2 |\bar{\mathbf{q}}|^2 + \Delta_b^2)^{1/2}, \quad (9)$$

spin operator	meson analog	$I$	$I_3$	type of spin
$c_{i,d+}^\dagger \boldsymbol{\sigma} c_{i,d+} + c_{i,d-}^\dagger \boldsymbol{\sigma} c_{i,d-}$	$\omega$	0	0	true
$c_{i,d+}^\dagger \boldsymbol{\sigma} c_{i,d+} - c_{i,d-}^\dagger \boldsymbol{\sigma} c_{i,d-}$	$\pi^0$	1	0	hidden
$c_{i,d+}^\dagger \boldsymbol{\sigma} c_{i,d-}$	$\pi^+$	1	+1	hidden
$c_{i,d-}^\dagger \boldsymbol{\sigma} c_{i,d+}$	$\pi^-$	1	-1	hidden

TABLE I: List of spin-excitation operators according to isospin. Above,  $\boldsymbol{\sigma}$  denotes the Pauli matrices for spin, and  $I$  and  $I_3$  denote the isospin quantum numbers. Summation over spin indices is implicit. Meson analogs are obtained by identifying the  $d+$  orbital with the  $u$  quark and the  $d-$  orbital with the  $d$  quark.

hidden spin operator	isospin quantization axis	reference
$c_{i,d_{xz}}^\dagger \boldsymbol{\sigma} c_{i,d_{xz}} - c_{i,d_{yz}}^\dagger \boldsymbol{\sigma} c_{i,d_{yz}}$	$I_1$	none
$c_{i,d_{xz}}^\dagger \boldsymbol{\sigma} c_{i,d_{yz}} + c_{i,d_{yz}}^\dagger \boldsymbol{\sigma} c_{i,d_{xz}}$	$I_2$	Berg, Metlitski and Sachdev (2012)
$i(c_{i,d_{xz}}^\dagger \boldsymbol{\sigma} c_{i,d_{yz}} - c_{i,d_{yz}}^\dagger \boldsymbol{\sigma} c_{i,d_{xz}})$	$I_3$	Rodriguez (2017)

TABLE II: List of hidden spin-excitation operators by isospin quantization axis. Summation over spin indices is implicit. Examples of where such hidden spin excitations appear in the literature are also listed. Note: the spin operator in the second row ( $I_2$ ) is diagonal in the orbital basis rotated by 45 degrees about the  $z$  axis;  $c_{i,d_{x'z}}^\dagger \boldsymbol{\sigma} c_{i,d_{x'z}} - c_{i,d_{y'z}}^\dagger \boldsymbol{\sigma} c_{i,d_{y'z}}$ , where  $x' = (x + y)/\sqrt{2}$  and  $y' = (-x + y)/\sqrt{2}$ .

where  $\mathbf{q} = \bar{\mathbf{q}} + \mathbf{Q}_{\text{AF}}$ . The velocity of the hidden spinwaves is given by  $c_b = (\rho_s/\chi_\perp)^{1/2}$ , while the spin gap  $\Delta_b$  is null when the hSDW state shows long-range order. It can be demonstrated that the spin  $s_1$  is equal to the spin per orbital in the local-moment limit described by the two-orbital Heisenberg model<sup>40</sup>. (See Appendix A.) Also, an analysis of the two-orbital extended Hubbard model<sup>31</sup> within the random phase approximation (RPA) finds that  $s_1$  is equal to the sub-lattice magnetization per orbital in the hSDW state<sup>41</sup>.

### III. ELIASHBERG THEORY

After adding on-iron-site Coulomb repulsion and magnetic frustration from superexchange via the selenium atoms to the electron hopping Hamiltonian (1), the author and

Melendrez recently showed that the hSDW state, with opposing Néel antiferromagnet order over the square lattice of iron atoms per  $d\pm$  orbital, is stable within the mean-field approximation at perfect nesting<sup>31</sup>. (See Fig. 1.) And after developing an Eliashberg theory in the particle-hole channel, these authors then showed that coupling to hidden spin fluctuations, (8) and (9), shifts the two electronic bands by an equal and opposite energy, leading to electron/hole Fermi surface pockets at the corner of the folded (two-iron) Brillouin zone. They also notably found that the spectral weight,  $1/Z$ , tends to zero at the new Fermi surface pockets.

Berg, Metlitski and Sachdev have performed determinant quantum Monte Carlo (DQMC) simulations on a similar model<sup>30</sup> that includes weak nesting of Fermi surfaces by the Néel wavevector  $\mathbf{Q}_{\text{AF}}$  and coupling to hidden spin fluctuations that are a superposition of those with isospin quantum numbers  $I_3 = +1$  and  $-1$ . (See Tables I and II.) They find a quantum-critical phase transition at low temperature between a hSDW and an  $D$ -wave superconductor, with Cooper pairs on nominal  $x$  versus  $y$  orbitals that alternate in sign between them. Below, we will show that a similar quantum-critical phase transition exists upon electron doping of the hSDW state considered here, with isospin quantum number  $I_3 = 0$  instead. In particular, an Eliashberg theory in the conventional particle-particle channel<sup>42–45</sup> will be revealed for electron-doped states that exhibit only short-range hSDW order. It predicts Cooper pairs that show  $S$ -wave symmetry, however.

### A. Hidden Spin Fluctuations and Interaction with Electrons

In the hidden Néel state considered here, with spontaneous symmetry breaking along the  $z$  axis, the propagator for spinwaves is given by

$$\left\langle \frac{1}{\sqrt{2}}m^+(\pi)\frac{1}{\sqrt{2}}m^-(\pi) \right\rangle \Big|_{\mathbf{q},\omega} = iD(\mathbf{q}, \omega), \quad (10)$$

with its form set by (8) and (9). We shall henceforth assume that the spin gap  $\Delta_b$  grows in a continuous fashion from zero upon crossing the quantum critical point. Electron doping from half filling shall be one of the principal tuning parameters for the quantum-critical phase transition. (Cf. Fig. 6.) Spin isotropy is recovered upon crossing the quantum critical point, however. It dictates the form

$$\left\langle \frac{1}{\sqrt{2}}m^{(z)}(\pi)\frac{1}{\sqrt{2}}m^{(z)}(\pi) \right\rangle \Big|_{\mathbf{q},\omega} = \frac{1}{2}iD(\mathbf{q}, \omega), \quad (11)$$

for the nature of hidden spin fluctuations along the  $z$  axis at  $\Delta_b > 0$ .

As was mentioned earlier, an extended Hubbard model over the square lattice of iron atoms in FeSe that shows perfect nesting of the Fermi surfaces (Fig. 1) harbors a hSDW state when magnetic frustration is present<sup>31</sup>. A mean field theory approximation of the extended Hubbard model implies an isotropic interaction between spin fluctuations and electrons of the form  $H_{e\text{-hsw}} = -\sum_i \sum_\alpha U(\pi) \mathbf{m}_{i,\alpha} \cdot 2\mathbf{S}_{i,\alpha}$ , where

$$U(\pi) = U_0 + \frac{1}{2}J_0. \quad (12)$$

Here,  $U_0$  is the on-site repulsive energy cost for the formation of a spin singlet on the  $d+$  orbital or on the  $d-$  orbital, while  $J_0$  is the (ferromagnetic) Hund's Rule spin-exchange coupling constant between these two orbitals. (See Appendix A.) The transverse contributions yield the interaction  $H_{e\text{-hsw}}^{(xy)} = -\sum_i \sum_\alpha U(\pi)(m_{i,\alpha}^+ S_{i,\alpha}^- + m_{i,\alpha}^- S_{i,\alpha}^+)$ , while the longitudinal contributions yield the interaction  $H_{e\text{-hsw}}^{(z)} = -\sum_i \sum_\alpha U(\pi)m_{i,\alpha}^{(z)} 2S_{i,\alpha}^{(z)}$ . In the basis of electron energy bands, they yield the following contribution to the Hamiltonian due to the interaction of electrons with hidden spin fluctuations:

$$H_{e\text{-hsw}}^{(xy)} = -\frac{1}{\sqrt{2}} \frac{U(\pi)}{a\mathcal{N}^{1/2}} \sum_{\mathbf{k}} \sum_{\mathbf{k}'} \sum_n [m^+(\pi, \mathbf{q}) c_{\downarrow}^\dagger(\bar{n}, \bar{\mathbf{k}}') c_{\uparrow}(n, \mathbf{k}) \mathcal{M}_{n,\mathbf{k};\bar{n},\bar{\mathbf{k}}'} + \text{h.c.}] \quad (13)$$

and

$$H_{e\text{-hsw}}^{(z)} = -\frac{1}{\sqrt{2}} \frac{U(\pi)}{a\mathcal{N}^{1/2}} \sum_{\mathbf{k}} \sum_{\mathbf{k}'} \sum_n \sum_s m^{(z)}(\pi, \mathbf{q}) c_s^\dagger(\bar{n}, \bar{\mathbf{k}}') c_s(n, \mathbf{k}) \cdot \mathcal{M}_{n,\mathbf{k};\bar{n},\bar{\mathbf{k}}'}(\text{sgn } s), \quad (14)$$

where  $\mathbf{q} = \mathbf{k} - \bar{\mathbf{k}}'$  is the momentum transfer, with  $\bar{\mathbf{k}}' = \mathbf{k}' + \mathbf{Q}_{\text{AF}}$ . Above,  $c_s^\dagger(n, \mathbf{k})$  and  $c_s(n, \mathbf{k})$  are electron creation and destruction operators for plane-wave states (5). The band indices  $n = 1$  and  $n = 2$  correspond, respectively, to anti-bonding ( $-$ ) planewaves in the  $d_{y(\delta)z}$  orbital and to bonding ( $+$ ) planewaves in the  $d_{x(\delta)z}$  orbital. Also,  $\bar{n}$  denotes the opposite band. The orbital matrix element that appears in (13) and in (14) is given by<sup>31</sup>

$$\mathcal{M}_{n,\mathbf{k};\bar{n},\bar{\mathbf{k}}'} = \pm \sin[\delta(\mathbf{k}) + \delta(\bar{\mathbf{k}}')]. \quad (15)$$

(See Appendix B.) Above, intra-band transitions are neglected because they do not show nesting.

We shall now apply the Nambu-Gorkov formalism for paired states<sup>44-47</sup>. It then becomes useful to write the above electron-hidden-spinwave interactions in terms of spinors:

$$H_{\text{e-hsw}}^{(xy)} = \mp \frac{1}{\sqrt{2}} \frac{U(\pi)}{a\mathcal{N}^{1/2}} \sum_{\mathbf{k}} \sum_{\mathbf{k}'} [m^+(\pi, \mathbf{q}) C_n^\dagger(\bar{\mathbf{k}}') \tau_3 \bar{C}_n(\mathbf{k}) \sin[\delta(\mathbf{k}) + \delta(\mathbf{k}')] + \text{h.c.}], \quad (16)$$

and

$$H_{\text{e-hsw}}^{(z)} = \mp \frac{1}{\sqrt{2}} \frac{U(\pi)}{a\mathcal{N}^{1/2}} \sum_{\mathbf{k}} \sum_{\mathbf{k}'} \sum_n m^{(z)}(\pi, \mathbf{q}) C_n^\dagger(\bar{\mathbf{k}}') \tau_0 C_n(\mathbf{k}) \cdot \sin[\delta(\mathbf{k}) + \delta(\mathbf{k}')], \quad (17)$$

with

$$C_n(\mathbf{k}) = \begin{bmatrix} c_\uparrow(n, \mathbf{k}) \\ c_\downarrow^\dagger(n, -\mathbf{k}) \end{bmatrix} \quad (18)$$

and

$$\bar{C}_n(\mathbf{k}) = \begin{bmatrix} c_\downarrow(n, \mathbf{k}) \\ c_\uparrow^\dagger(n, -\mathbf{k}) \end{bmatrix}. \quad (19)$$

Above,  $\tau_3$  is the Pauli matrix along the  $z$  axis, and  $\tau_0$  is the  $2 \times 2$  identity matrix. Also, the explicit matrix element (15)  $\mathcal{M}_{n, \mathbf{k}; \bar{n}, \bar{\mathbf{k}}'}$  has been substituted in. (See Appendix B.) It is important to point out that the band index  $n$  is *fixed* in expression (16) for  $H_{\text{e-hsw}}^{(xy)}$  above. The  $n = 1$  and the  $n = 2$  expressions are equivalent.

## B. Electron Propagators and Eliashberg Equations

Let  $C_n(\mathbf{k}, t)$  and  $\bar{C}_n(\mathbf{k}, t)$  denote the time evolution of the Nambu-Gorkov spinors,  $C_n(\mathbf{k})$  and  $\bar{C}_n(\mathbf{k})$ , and let  $C_n^\dagger(\mathbf{k}, t)$  and  $\bar{C}_n^\dagger(\mathbf{k}, t)$  denote the time evolution of their conjugates,  $C_n^\dagger(\mathbf{k})$  and  $\bar{C}_n^\dagger(\mathbf{k})$ . The Nambu-Gorkov electron propagators are then the Fourier transforms  $iG_n(\mathbf{k}, \omega) = \int dt_{1,2} e^{i\omega t_{1,2}} \langle T[C_n(\mathbf{k}, t_1) C_n^\dagger(\mathbf{k}, t_2)] \rangle$  and  $i\bar{G}_n(\mathbf{k}, \omega) = \int dt_{1,2} e^{i\omega t_{1,2}} \langle T[\bar{C}_n(\mathbf{k}, t_1) \bar{C}_n^\dagger(\mathbf{k}, t_2)] \rangle$ , where  $t_{1,2} = t_1 - t_2$ , and where  $T$  is the time-ordering operator. They are  $2 \times 2$  matrices. In the absence of interactions, their matrix inverses are then given by

$$G_{0n}^{-1}(\mathbf{k}, \omega) = \omega \tau_0 - [\varepsilon_n(\mathbf{k}) - \mu_0] \tau_3. \quad (20)$$

Following the standard prescription<sup>44,45</sup>, let us next assume that the matrix inverse of the Nambu-Gorkov Greens function takes the form

$$G_n^{-1}(\mathbf{k}, \omega) = Z_n(\mathbf{k}, \omega)\omega \tau_0 - [\varepsilon_n(\mathbf{k}) - \mu_n] \tau_3 - Z_n(\mathbf{k}, \omega)\Delta_n(\mathbf{k}) \tau_1. \quad (21)$$

Here,  $Z_n(\mathbf{k}, \omega)$  is the wavefunction renormalization,  $\Delta_n(\mathbf{k})$  is the quasi-particle gap, and  $\mu_n - \mu_0$  is the shift in the energy band. Matrix inversion of (21) yields the Nambu-Gorkov Greens function<sup>44-47</sup>  $G = \sum_{\mu=0}^3 G^{(\mu)}\tau_\mu$ , with components

$$\begin{aligned} G_n^{(0)} &= \frac{1}{2Z_n} \left( \frac{1}{\omega - E_n} + \frac{1}{\omega + E_n} \right), \\ G_n^{(1)} &= \frac{1}{2Z_n} \left( \frac{1}{\omega - E_n} - \frac{1}{\omega + E_n} \right) \frac{\Delta_n}{E_n}, \\ G_n^{(3)} &= \frac{1}{2Z_n} \left( \frac{1}{\omega - E_n} - \frac{1}{\omega + E_n} \right) \frac{\varepsilon_n - \mu_n}{Z_n E_n}, \end{aligned} \quad (22)$$

and  $G_n^{(2)} = 0$ . Above, the excitation energy is

$$E_n(\mathbf{k}, \omega) = \sqrt{\left[ \frac{\varepsilon_n(\mathbf{k}) - \mu_n}{Z_n(\mathbf{k}, \omega)} \right]^2 + \Delta_n^2(\mathbf{k})}. \quad (23)$$

Last, because the spinors (18) and (19) are related by spin flip, and because we assume spin singlet Cooper pairs, then  $\bar{G}$  is obtained from  $G$  by the replacement  $\Delta_n \rightarrow -\Delta_n$ . This yields  $\bar{G}_n^{(0)} = G_n^{(0)}$ ,  $\bar{G}_n^{(1)} = -G_n^{(1)}$ ,  $\bar{G}_n^{(2)} = -G_n^{(2)}$ , and  $\bar{G}_n^{(3)} = G_n^{(3)}$ .

To obtain the Eliashberg equations, recall first the definition of the self-energy correction per band:  $G_n^{-1} = G_0^{-1} - \Sigma_n$ . Comparison of the inverse Greens functions (20) and (21) then yields the following expression for it<sup>44,45</sup>:

$$\Sigma_n(\mathbf{k}, \omega) = [1 - Z_n(\mathbf{k}, \omega)]\omega \tau_0 - (\mu_n - \mu_0) \tau_3 + Z_n(\mathbf{k}, \omega)\Delta_n(\mathbf{k}) \tau_1. \quad (24)$$

Next, we neglect vertex corrections from the electron-hidden-spinwave interactions, (16) and (17). Figure 3 displays the resulting self-consistent approximation. This approximation will be justified *a posteriori* in the next section. The self-energy correction is then given by

$$\begin{aligned} \Sigma_n(\mathbf{k}, \omega) &= i \int_{\text{BZ}} \frac{d^2 k'}{(2\pi)^2} \int_{-\infty}^{+\infty} \frac{d\omega'}{2\pi} \frac{U^2(\pi)}{2} \sin^2[\delta(\mathbf{k}) + \delta(\mathbf{k}')] D(\mathbf{q}, q_0) \cdot \\ &\quad \cdot [\tau_3 \bar{G}_n(\bar{\mathbf{k}}', \omega') \tau_3 + \frac{1}{2} G_n(\bar{\mathbf{k}}', \omega')], \end{aligned} \quad (25)$$

with  $q_0 = \omega - \omega'$ , and with  $\mathbf{q} = \mathbf{k} - \bar{\mathbf{k}}'$ . Observe, finally, that  $\tau_3\tau_\mu\tau_3 = \text{sgn}_\mu\tau_\mu$ , where  $\text{sgn}_0 = +1 = \text{sgn}_3$ , and where  $\text{sgn}_1 = -1 = \text{sgn}_2$ . Identifying expressions (24) and (25) for the self-energy corrections then yields the following self-consistent Eliashberg equations at zero temperature:

$$\begin{aligned}
-[Z_n(\mathbf{k}, \omega) - 1]\omega &= + \int_{\text{BZ}} \frac{d^2k'}{(2\pi)^2} i \int_{-\infty}^{+\infty} \frac{d\omega'}{2\pi} \frac{U^2(\pi)}{2} \sin^2[\delta(\mathbf{k}) + \delta(\mathbf{k}')] \cdot \\
&\quad \cdot D(\mathbf{q}, q_0) [\bar{G}_n^{(0)}(\bar{\mathbf{k}}', \omega') + \frac{1}{2}G_n^{(0)}(\bar{\mathbf{k}}', \omega')], \\
\mu_0 - \mu_n &= + \int_{\text{BZ}} \frac{d^2k'}{(2\pi)^2} i \int_{-\infty}^{+\infty} \frac{d\omega'}{2\pi} \frac{U^2(\pi)}{2} \sin^2[\delta(\mathbf{k}) + \delta(\mathbf{k}')] \cdot \\
&\quad \cdot D(\mathbf{q}, q_0) [\bar{G}_n^{(3)}(\bar{\mathbf{k}}', \omega') + \frac{1}{2}G_n^{(3)}(\bar{\mathbf{k}}', \omega')], \\
Z_n(\mathbf{k}, \omega)\Delta_n(\mathbf{k}, \omega) &= - \int_{\text{BZ}} \frac{d^2k'}{(2\pi)^2} i \int_{-\infty}^{+\infty} \frac{d\omega'}{2\pi} \frac{U^2(\pi)}{2} \sin^2[\delta(\mathbf{k}) + \delta(\mathbf{k}')] \cdot \\
&\quad \cdot D(\mathbf{q}, q_0) [\bar{G}_n^{(1)}(\bar{\mathbf{k}}', \omega') - \frac{1}{2}G_n^{(1)}(\bar{\mathbf{k}}', \omega')].
\end{aligned} \tag{26}$$

The Greens functions above are listed in (22) and below (23).

Last, it becomes useful to write the propagator for hidden spinwaves (8) as

$$D(\mathbf{q}, \omega) = \frac{(2s_1)^2}{\chi_\perp} \frac{1}{2\omega_b(\mathbf{q})} \left[ \frac{1}{\omega - \omega_b(\mathbf{q})} - \frac{1}{\omega + \omega_b(\mathbf{q})} \right]. \tag{27}$$

The integrals over frequency in the Eliashberg equations above (26) can be evaluated by going into the complex plane. Specifically, make the replacement  $E_n \rightarrow E_n - i\eta$  in the poles of the electron Greens functions (22), make the replacement  $\omega_b(\mathbf{q}) \rightarrow \omega_b(\mathbf{q}) - i\eta$  in the poles of the spin-wave propagator (27), and regularize the contour integrals by including the factor  $e^{i\omega'\tau}$  in the integrands. Here,  $\eta \rightarrow 0+$  and  $\tau \rightarrow 0+$ . Application of Cauchy's residue theorem yields the following result, which is equivalent to Brillouin-Wigner second-order

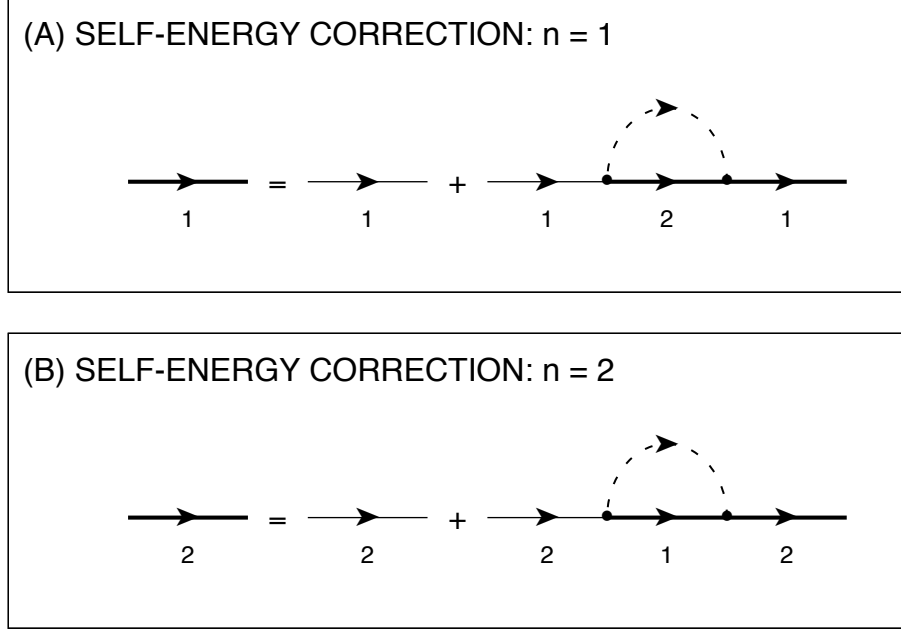


FIG. 3: Feynman diagrams for electron propagator with purely inter-band scattering, in the absence of vertex corrections.

perturbation theory<sup>44</sup>:

$$\begin{aligned}
[Z_n(\mathbf{k}, \omega) - 1]\omega &= \frac{3}{2} \int_{\text{BZ}} \frac{d^2 k'}{(2\pi)^2} U^2(\pi) \frac{s_1^2}{\chi_\perp} \frac{\sin^2[\delta(\mathbf{k}) + \delta(\mathbf{k}')] }{Z_{\bar{n}}(\bar{\mathbf{k}}', \omega')} \\
&\cdot \frac{1}{2\omega_b(\mathbf{q})} \left[ \frac{1}{\omega_b(\mathbf{q}) + E_{\bar{n}}(\bar{\mathbf{k}}') - \omega} - \frac{1}{\omega_b(\mathbf{q}) + E_{\bar{n}}(\bar{\mathbf{k}}') + \omega} \right], \\
\mu_0 - \mu_n &= -\frac{3}{2} \int_{\text{BZ}} \frac{d^2 k'}{(2\pi)^2} U^2(\pi) \frac{s_1^2}{\chi_\perp} \frac{\sin^2[\delta(\mathbf{k}) + \delta(\mathbf{k}')] }{Z_{\bar{n}}(\bar{\mathbf{k}}', \omega')} \frac{\varepsilon_{\bar{n}}(\bar{\mathbf{k}}') - \mu_{\bar{n}}}{Z_{\bar{n}}(\bar{\mathbf{k}}', \omega') E_{\bar{n}}(\bar{\mathbf{k}}')} \\
&\cdot \frac{1}{2\omega_b(\mathbf{q})} \left[ \frac{1}{\omega_b(\mathbf{q}) + E_{\bar{n}}(\bar{\mathbf{k}}') - \omega} + \frac{1}{\omega_b(\mathbf{q}) + E_{\bar{n}}(\bar{\mathbf{k}}') + \omega} \right], \\
Z_n(\mathbf{k}, \omega) \Delta_n(\mathbf{k}, \omega) &= -\frac{3}{2} \int_{\text{BZ}} \frac{d^2 k'}{(2\pi)^2} U^2(\pi) \frac{s_1^2}{\chi_\perp} \frac{\sin^2[\delta(\mathbf{k}) + \delta(\mathbf{k}')] }{Z_{\bar{n}}(\bar{\mathbf{k}}', \omega')} \frac{\Delta_{\bar{n}}(\bar{\mathbf{k}}', \omega')}{E_{\bar{n}}(\bar{\mathbf{k}}')} \\
&\cdot \frac{1}{2\omega_b(\mathbf{q})} \left[ \frac{1}{\omega_b(\mathbf{q}) + E_{\bar{n}}(\bar{\mathbf{k}}') - \omega} + \frac{1}{\omega_b(\mathbf{q}) + E_{\bar{n}}(\bar{\mathbf{k}}') + \omega} \right].
\end{aligned} \tag{28}$$

Above<sup>45</sup>,  $\omega' = E_{\bar{n}}(\bar{\mathbf{k}}')$ . In the previous, the momentum integrals have been shifted by  $\mathbf{Q}_{\text{AF}}$

for convenience in order to exploit perfect nesting (7). Also, the prefactors of 3/2 above are a result of the identities between  $G_n^{(\mu)}$  and  $\bar{G}_n^{(\mu)}$  that are listed below (23). We shall now find solutions to the Eliashberg equations.

#### IV. LIFSHITZ TRANSITION AND PAIRING INSTABILITY AT THE FERMI SURFACE

Henceforth, assume isotropic ( $S$ -wave) Cooper pairs. Following the standard procedure<sup>44,45</sup>, let us multiply both sides of the Eliashberg equations (28) by  $\delta[\varepsilon_n(\mathbf{k}) - \mu_n]/D_n(\mu_n)$  and integrate in momentum over the first Brillouin zone. The Eliashberg equations (28) thereby reduce to

$$(Z_n - 1)\omega = \int_{-W_{\text{bottom}}(\bar{n})}^{+W_{\text{top}}(\bar{n})} d\varepsilon' Z_{\bar{n}}'^{-1} \int_0^\infty d\Omega U^2 F_0^{(n,\bar{n})}(\Omega; \mu_n, \mu_{\bar{n}}) \cdot \frac{1}{2} \left[ \frac{1}{\Omega + E_{\bar{n}}' - \omega} - \frac{1}{\Omega + E_{\bar{n}}' + \omega} \right], \quad (29a)$$

$$\mu_0 - \mu_n = - \int_{-W_{\text{bottom}}(\bar{n})}^{+W_{\text{top}}(\bar{n})} d\varepsilon' Z_{\bar{n}}'^{-1} \int_0^\infty d\Omega U^2 F_0^{(n,\bar{n})}(\Omega; \mu_n, \mu_{\bar{n}}) \frac{\varepsilon' - \mu_{\bar{n}}}{Z_{\bar{n}}' E_{\bar{n}}'} \cdot \frac{1}{2} \left[ \frac{1}{\Omega + E_{\bar{n}}' - \omega} + \frac{1}{\Omega + E_{\bar{n}}' + \omega} \right], \quad (29b)$$

$$Z_n \Delta_n = - \int_{-W_{\text{bottom}}(\bar{n})}^{+W_{\text{top}}(\bar{n})} d\varepsilon' Z_{\bar{n}}'^{-1} \int_0^\infty d\Omega U^2 F_0^{(n,\bar{n})}(\Omega; \mu_n, \mu_{\bar{n}}) \frac{\Delta_{\bar{n}}'}{E_{\bar{n}}'} \cdot \frac{1}{2} \left[ \frac{1}{\Omega + E_{\bar{n}}' - \omega} + \frac{1}{\Omega + E_{\bar{n}}' + \omega} \right], \quad (29c)$$

where

$$U^2 F_0^{(n,\bar{n})}(\Omega; \varepsilon, \varepsilon') = \frac{1}{D_n(\varepsilon)} \frac{3}{2} \int \frac{d^2 k}{(2\pi)^2} \int \frac{d^2 k'}{(2\pi)^2} U^2(\pi) \frac{s_1^2 \sin^2[\delta(\mathbf{k}) + \delta(\mathbf{k}')] }{\chi_\perp \omega_b(\mathbf{q})} \cdot \delta[\varepsilon_n(\mathbf{k}) - \varepsilon] \delta[\varepsilon_{\bar{n}}(\bar{\mathbf{k}}') - \varepsilon'] \delta[\omega_b(\mathbf{q}) - \Omega], \quad (30)$$

and where

$$E_{\bar{n}}' = [(\varepsilon' - \mu_{\bar{n}})/Z_{\bar{n}}']^2 + \Delta_{\bar{n}}'^2)^{1/2}.$$

Here, the wavefunction renormalization and the gap are averaged over the new Fermi surface:  $Z_n(\mathbf{k}, \omega) \rightarrow [D_n(\mu_n)]^{-1} (2\pi)^{-2} \int_{\text{BZ}} d^2 k Z_n(\mathbf{k}, \omega) \delta[\varepsilon_n(\mathbf{k}) - \mu_n]$ , and  $Z_n \Delta_n(\mathbf{k}, \omega) \rightarrow$

$[D_n(\mu_n)]^{-1}(2\pi)^{-2} \int_{\text{BZ}} d^2k Z_n \Delta_n(\mathbf{k}, \omega) \delta[\varepsilon_n(\mathbf{k}) - \mu_n]$ . The neglect of angular dependence is exact for circular Fermi surface pockets at  $(\pi/a, 0)$  and at  $(0, \pi/a)$ . This occurs for  $\mu_2$  near the upper band edge of  $\varepsilon_+(\mathbf{k})$  and for  $\mu_1$  near the lower band edge of  $\varepsilon_-(\mathbf{k})$ , in the absence of nearest-neighbor intra-orbital hopping,  $t_1^\parallel \rightarrow 0$ . Above, we have also approximated the function  $U^2 F_0^{(n, \bar{n})}(\Omega; \mu_n, \varepsilon')$  of  $\varepsilon'$  by its value at the renormalized chemical potential,  $U^2 F_0^{(n, \bar{n})}(\Omega; \mu_n, \mu_{\bar{n}})$ .

### A. Half Filling

One of the central aims of this paper is to reveal a Lifshitz transition from the Fermi surfaces depicted by Fig. 1 to electron/hole pockets at the corner of the folded (two-iron) Brillouin zone. Let us start at half filling:  $\mu_0 = 0$ . The Fermi surfaces are then set by  $\varepsilon_-(\mathbf{k}) = -\nu$  and  $\varepsilon_+(\mathbf{k}) = +\nu$ , where  $\mu_1 = -\nu$  and  $\mu_2 = +\nu$  are the shifts in energy of the anti-bonding ( $-$ ) band and of the bonding ( $+$ ) band, respectively. Because of perfect nesting (7), we have  $\varepsilon_\pm(\bar{\mathbf{k}}) - \mu_\pm = \mu_\mp - \varepsilon_\mp(\mathbf{k})$ . The Eliashberg equations (28) are then symmetric with respect to the permutation of the band indices. We thereby have  $Z_1 = Z_2$  and  $\Delta_1 = -\Delta_2$ . These unknowns, in addition to  $\nu$ , are to be determined by the Eliashberg equations (29a)-(29c).

The effective spectral weight of the hidden spinwaves,  $U^2 F_0^{(2,1)}(\Omega; \mu_2, \mu_1)$ , can be evaluated by choosing coordinates for the momentum of the electron,  $(k_\parallel, k_\perp)$ , that are respectively parallel and perpendicular to the Fermi surface of the bonding band (FS $_+$ ):  $\nu = \varepsilon_+(\mathbf{k})$ . And because of perfect nesting (7), it coincides with the Fermi surface of the anti-bonding ( $-$ ) band after the momentum is shifted by  $\mathbf{Q}_{\text{AF}}$ :  $\mathbf{k}' \rightarrow \bar{\mathbf{k}}'$ . (See Figs. 1 and 4.) This yields the intermediate result

$$U^2 F_0^{(2,1)}(\Omega; \mu_2, \mu_1) = \frac{1}{D_+(\nu)} \frac{3}{2} \oint_{\text{FS}_+} \frac{dk_\parallel}{(2\pi)^2} \oint_{\text{FS}_+} \frac{dk'_\parallel}{(2\pi)^2} U^2(\pi) \frac{s_1^2}{\chi_\perp} \frac{1}{\Omega} \cdot \frac{\sin^2[\delta(\mathbf{k}) + \delta(\mathbf{k}')] }{|\mathbf{v}_+(\mathbf{k})||\mathbf{v}_+(\mathbf{k}')|} \delta[\omega_b(\mathbf{q}) - \Omega], \quad (31)$$

where  $\mathbf{v}_+ = \partial\varepsilon_+/\partial\mathbf{k}$  is the group velocity. Yet the dispersion of the spectrum of hidden spinwaves follows  $\omega_b(\mathbf{q}) = \sqrt{c_b^2|\bar{\mathbf{q}}|^2 + \Delta_b^2}$  at the long-wavelength limit. Making the approximation  $|\bar{\mathbf{q}}| \cong |k_\parallel - k'_\parallel|$  at small momentum transfers then yields the following dependence on frequency for the effective spectral weight:  $U^2 F_0^{(2,1)}(\Omega; \mu_2, \mu_1) = \epsilon_E(\nu)/\sqrt{\Omega^2 - \Delta_b^2}$  for

$\Omega > \Delta_b$ , with a constant pre-factor

$$\epsilon_E(\nu) = \frac{1}{D_+(\nu)} \frac{3}{2} \oint_{\text{FS}_+} \frac{dk_{\parallel}}{(2\pi)^4} U^2(\pi) \frac{s_1^2}{\chi_{\perp}} \frac{[\sin 2\delta(\mathbf{k})]^2}{c_b |\mathbf{v}_+(\mathbf{k})|^2}, \quad (32)$$

while  $U^2 F_0^{(2,1)}(\Omega; \mu_2, \mu_1) = 0$  for  $0 \leq \Omega \leq \Delta_b$ .

Next, let us assume the trivial solution for the gap equations (29c):  $\Delta_n = 0$ . It will be shown *a posteriori* that this is indeed the case. We can now find solutions to the remaining Eliashberg equations (29a) and (29b). In particular, assume that the equal and opposite shift in energy  $\nu$  of the bands lies near the upper edge  $W_{\text{top}}$  of the bonding band  $\varepsilon_+(\mathbf{k})$  at  $(\pi/a, 0)$  and at  $(0, \pi/a)$ . (Cf. Fig. 2.) Figure 4 displays the Fermi surfaces in such case. Substituting in the previous result for the dependence on frequency of  $U^2 F_0^{(2,1)}(\Omega; \mu_2, \mu_1)$  yields the first Eliashberg equation:

$$\omega(Z - 1) = \frac{\epsilon_E}{2} \int_{\Delta_b}^{\omega_{\text{uv}}} \frac{d\Omega}{\sqrt{\Omega^2 - \Delta_b^2}} \ln \left| \frac{\Omega + \omega}{\Omega - \omega} \cdot \frac{W/Z + \Omega - \omega}{W/Z + \Omega + \omega} \right|. \quad (33)$$

Here, we have reversed the order of integration:  $[-W_{\text{bottom}}, +W_{\text{top}}]$  is the range of integration over  $\varepsilon'$  in (29a), where  $-W_{\text{bottom}}$  and  $+W_{\text{top}}$  denote the minimum and the maximum of the band  $\varepsilon_+(\mathbf{k})$ , respectively. Its bandwidth is then  $W = W_{\text{bottom}} + W_{\text{top}}$ . Also,  $\omega_{\text{uv}}$  is an ultra-violet cutoff in frequency for the hidden spinwaves. Expanding the integrand above to linear order in frequency  $\omega$  then yields ultimately the Eliashberg equation for the wavefunction renormalization at the Fermi level,  $\omega = 0$ :

$$Z - 1 = \epsilon_E \int_{\Delta_b}^{\omega_{\text{uv}}} \frac{d\Omega}{\sqrt{\Omega^2 - \Delta_b^2}} \left( \frac{1}{\Omega} - \frac{1}{W/Z + \Omega} \right). \quad (34)$$

Likewise, inverting the order of integration of the second Eliashberg equation (29b) for the inter-band energy shift yields

$$\nu = \epsilon_E \int_{\Delta_b}^{\omega_{\text{uv}}} \frac{d\Omega}{\sqrt{\Omega^2 - \Delta_b^2}} \ln \left| \frac{W/Z + \Omega}{\Omega} \right| \quad (35)$$

at  $\omega = 0$ .

Long-range hSDW order exists at half filling because of perfect nesting (Fig. 4). We must therefore approach criticality:  $\Delta_b \rightarrow 0$ . The Eliashberg equations (34) and (35) predict a Lifshitz transition of the topology of the Fermi surface that is confirmed by making the following change of variables:  $Z = \varepsilon_E/\Delta_b$  and  $\cosh x = \Omega/\Delta_b$ . At criticality,  $\Delta_b \rightarrow 0$ , they yield Eliashberg equations

$$\frac{\varepsilon_E}{W} = \frac{\epsilon_E}{W} [I(0) - I(y)] \quad \text{and} \quad \frac{\nu}{W} = \frac{\epsilon_E}{W} J(y), \quad (36)$$

where

$$I(y) = \int_0^\infty dx \frac{1}{y + \cosh x}, \quad (37a)$$

$$J(y) = \int_0^\infty dx \ln \left( 1 + \frac{y}{\cosh x} \right), \quad (37b)$$

with  $y = W/\varepsilon_E$ . The quadratic dependence of  $\varepsilon_E$  on Hubbard repulsion (32) implies that  $\nu$  saturates to  $W_{\text{top}}$  as  $U(\pi)$  diverges. (See Fig. 4.) Dividing the two Eliashberg equations (36), we then get the transcendental equation

$$y^{-1} \frac{W}{W_{\text{top}}} = \frac{I(0) - I(y)}{J(y)} \quad (38)$$

as  $U(\pi) \rightarrow \infty$ . Notice that  $y$  depends only on  $W/W_{\text{top}} = (t_1^\parallel + t_1^\perp)/t_1^\perp$  in such case. The definite integrals (37a) and (37b) can be evaluated in closed form. (See Appendix C.) Numerical solutions to the transcendental equation (38) are listed in Table IV.

Last, what is the energy gap of the superconducting state at half filling, approaching criticality? Again, the antisymmetry displayed by the gap equations (29c) at half filling with respect to the permutation of band indices implies perfect  $S^{+-}$  Cooper pairing:  $\Delta_1 = +\Delta$  and  $\Delta_2 = -\Delta$ . (Cf. refs.<sup>48, 49, and 50</sup>.) The last Eliashberg equation (29c) then reads

$$Z\Delta = \int_{-W_{\text{bottom}}}^{+W_{\text{top}}} d\varepsilon' Z^{-1} \frac{\Delta'}{E'} \int_{\Delta_b}^{\omega_{\text{uv}}} d\Omega \frac{\varepsilon_E}{\sqrt{\Omega^2 - \Delta_b^2}} \frac{1}{\Omega + E'} \quad (39)$$

at the Fermi level,  $\omega = 0$ , where  $E' = \sqrt{[(\varepsilon' - \nu)/Z]^2 + \Delta'^2}$ . After again making the change of variable  $\Omega = \Delta_b \cosh(x)$ , the first integral over  $\Omega$  in (39) becomes

$$\lim_{\Delta_b \rightarrow 0} \int_0^\infty dx \frac{\varepsilon_E}{\Delta_b} \left[ \sqrt{\left( \frac{\varepsilon' - \nu}{\varepsilon_E} \right)^2 + \left( \frac{\Delta'}{\Delta_b} \right)^2} + \cosh x \right]^{-1} = \frac{\varepsilon_E}{\Delta'} \ln \left( 2 \frac{\Delta'}{\Delta_b} \right).$$

Here we have used  $\lim_{y \rightarrow \infty} I(y) = y^{-1} \ln(2y)$ . (See Appendix C.) Assume now the simple Bardeen-Cooper-Schrieffer (BCS) form for the frequency dependence of the gap<sup>44</sup>:

$$\Delta(\omega) = \begin{cases} \Delta_0 & \text{for } |\omega| < \omega_c, \\ 0 & \text{otherwise,} \end{cases} \quad (40)$$

but in the limit  $\omega_c \rightarrow 0$ . It is therefore consistent with the previous solutions for  $Z$  and for  $\nu$  in the normal state. The second integral over  $\varepsilon'$  in the gap equation (39) then becomes

$$\Delta_0 \int_{-\omega_c}^{+\omega_c} d\omega' (\omega'^2 + \Delta_0^2)^{-1/2} = 2\Delta_0 \sinh^{-1} \left( \frac{\omega_c}{\Delta_0} \right).$$

Here, we have made the change of variable  $\omega' = (\varepsilon' - \nu)/Z$ . Substituting in the form of the wavefunction renormalization  $Z = \varepsilon_E/\Delta_b$  into the left-hand side of the gap equation (39) plus some manipulation then yields

$$\frac{\Delta_0}{\sinh^{-1}\left(\frac{\omega_c}{\Delta_0}\right)} = \lim_{\Delta_b \rightarrow 0} 2 \frac{\varepsilon_E}{\varepsilon_E} \Delta_b \ln\left(2 \frac{\Delta_0}{\Delta_b}\right) = 0.$$

As expected, we therefore have a null gap due to superconductivity,  $\Delta_0 = 0$ , at half filling, at criticality.

Finally, the Eliashberg energy scale  $\varepsilon_E$  can be easily estimated in the case of small circular renormalized Fermi surface pockets<sup>31</sup>, which occurs as  $t_1^\parallel \rightarrow 0$ . In such case, it becomes convenient to re-express (32) as

$$\varepsilon_E(\nu) = \frac{3}{(2\pi)^3} \frac{U^2}{D_+(\nu)} \frac{s_1^2 k_F}{\chi_\perp c_b v_F^2}, \quad (41)$$

where  $U^2$  is the product of  $U^2(\pi)$  with the average of  $\sin^2(2\delta)$  around the hole-type Fermi surface pockets shown in Fig. 4. Here,  $k_F$  and  $v_F$  are the Fermi wavenumber and the Fermi velocity, respectively. They are given by  $k_F = a^{-1}(2\pi x_0)^{1/2}$ , where  $x_0$  denotes the concentration of electrons/holes in each Fermi surface pocket, and by  $v_F = 2t_1^\perp a^2 k_F$ . The solution to the Eliashberg equations (36) yields  $\varepsilon_E \cong W/3$ . (See Table IV.) Expression (41) then implies that the effective interaction strength scales as  $U \propto x_0^{1/4}$ . Further, expression (6b) yields the result  $\sin 2\delta(\mathbf{k}) \cong [(t_2^\perp/i)/2t_1^\perp](k_F a)^2 (\sin 2\phi)$ , where  $\phi$  is the angle that  $\mathbf{k}$  makes about the center of the Fermi surface pocket. The Eliashberg energy scale is thereby given explicitly by the following expression at criticality<sup>31</sup>, as  $t_1^\parallel \rightarrow 0$ :

$$\varepsilon_E = \frac{3}{32} \left(\frac{x_0}{2\pi}\right)^{3/2} \frac{U^2(\pi)}{a^2 D_+(\nu)} \frac{s_1^2}{a^2 \chi_\perp} \frac{|t_2^\perp|^2}{(c_b/a) |t_1^\perp|^4}. \quad (42)$$

The solution  $\varepsilon_E \cong W/3$  listed in Table IV then yields that the area of the electron/hole Fermi surface pockets shown in Fig. 4 is related to the Hubbard repulsion by  $U(\pi) \propto x_0^{-3/4}$ . We therefore conclude that the effective interaction strength  $U$  vanishes with the strength of the Hubbard repulsion<sup>31</sup> as  $U_0^{-1/3}$ . In the case where the spectrum  $\omega_b(\mathbf{q})$  of hidden spin fluctuations is *fixed*, this justifies the neglect of vertex corrections to the self-energy corrections shown by Fig. 3 at large Hubbard repulsion,  $U_0 \rightarrow \infty$ .

As on-site repulsion  $U_0$  grows strong, the Eliashberg equations (29a)-(29c) therefore predict a Lifshitz transition from unrenormalized Fermi surfaces shown in Fig. 1 to renormalized

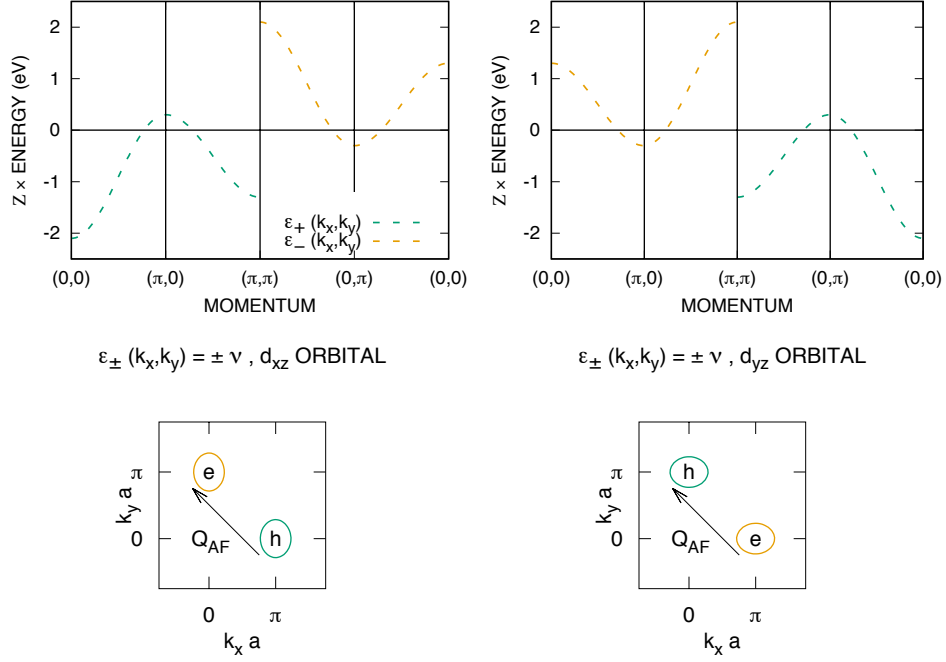


FIG. 4: Renormalized electron bands and Fermi surfaces at half filling after the Lifshitz transition from Fig. 1. The staggered band shift is  $\nu = 1.7$  eV. The orbital character is only approximate, although it becomes exact as the area of the Fermi surface pockets vanishes as  $U_0$  diverges.

Fermi surface pockets show in Fig. 4. The groundstate remains an hSDW at half filling due to nested Fermi surface pockets at the corner of the folded Brillouin zone. It must be emphasized, however, that the spectral weight of the renormalized Fermi surface pockets is vanishingly small:  $Z^{-1} = \Delta_b/\varepsilon_E \rightarrow 0$  at criticality,  $\Delta_b \rightarrow 0$ . This implies that the hSDW state at half filling is in fact a Mott insulator. It is also important to mention that these results for the Lifshitz transition confirm previous ones that start from the other side of the QCP at  $\Delta_b = 0$ . They were based on an Eliashberg theory in the particle-hole channel for the long-range ordered hSDW state<sup>31</sup>.

## B. Weak Electron Doping

We will now obtain solutions to the Eliashberg equations (28) at small deviations in the electron density from half filling. In the normal state,  $\Delta_1 = 0 = \Delta_2$ , the corresponding

equations for the wavefunction renormalizations and for the band shifts read

$$Z_n - 1 = \frac{3}{2} \int \frac{d^2 k'}{(2\pi)^2} U^2(\pi) \frac{s_1^2 \sin^2[\delta(\mathbf{k}) + \delta(\mathbf{k}')] }{\chi_\perp Z_{\bar{n}} \omega_b(\mathbf{q})} \cdot \frac{1}{[\omega_b(\mathbf{q}) + |\varepsilon_+(\mathbf{k}') - \nu_{\bar{n}}|/Z_{\bar{n}}]^2}, \quad (43a)$$

$$\nu_n - (\text{sgn } n)\mu_0 = \frac{3}{2} \int \frac{d^2 k'}{(2\pi)^2} U^2(\pi) \frac{s_1^2 \sin^2[\delta(\mathbf{k}) + \delta(\mathbf{k}')] }{\chi_\perp Z_{\bar{n}} \omega_b(\mathbf{q})} \cdot \frac{\text{sgn}[\nu_{\bar{n}} - \varepsilon_+(\mathbf{k}')] }{\omega_b(\mathbf{q}) + |\varepsilon_+(\mathbf{k}') - \nu_{\bar{n}}|/Z_{\bar{n}}}. \quad (43b)$$

Above,  $\nu_1 = -\mu_1$  and  $\nu_2 = +\mu_2$  are the staggered band shifts. Also, the identity

$$\sin[\delta(\mathbf{k}) + \delta(\mathbf{k}')] = \sin[\delta(\bar{\mathbf{k}}) + \delta(\bar{\mathbf{k}}')] \quad (44)$$

has been applied above in the case  $n = 1$  for the anti-bonding ( $-$ ) band. (See Appendix B.) Assume, in particular, that the chemical potential is positive, but small:  $\mu_0 \rightarrow 0+$ . Assume, next, a linear response  $\delta Z_1$  and  $\delta Z_2$  with respect to the wavefunction renormalization at half filling,  $Z_1 = Z$  and  $Z_2 = Z$ , along with a linear response  $\delta\nu_1$  and  $\delta\nu_2$  with respect to the staggered band shifts at half filling,  $\nu_1 = \nu$  and  $\nu_2 = \nu$ . Taking a variation of (43a) yields one linear equation per band,  $n = 1, 2$ . Adding and subtracting these yields the following linear relations in terms of even and odd variations with respect to half filling:

$$\begin{aligned} Z \delta Z(+) &= A \delta Z(+) - B \delta\nu(+), \\ 0 &= A \delta Z(-) - B \delta\nu(-), \end{aligned} \quad (45)$$

where  $\delta Z(\pm) = \frac{1}{2}(\delta Z_2 \pm \delta Z_1)$  and  $\delta\nu(\pm) = \frac{1}{2}(\delta\nu_2 \pm \delta\nu_1)$ . Here, we have constants

$$\begin{aligned} A &= \frac{3}{2} \int \frac{d^2 k'}{(2\pi)^2} U^2(\pi) \frac{s_1^2 \sin^2[\delta(\mathbf{k}) + \delta(\mathbf{k}')] }{\chi_\perp \omega_b(\mathbf{q})} \frac{1}{Z} \frac{|\varepsilon_+(\mathbf{k}') - \nu|/Z}{[\omega_b(\mathbf{q}) + |\varepsilon_+(\mathbf{k}') - \nu|/Z]^3}, \\ B &= \frac{3}{2} \int \frac{d^2 k'}{(2\pi)^2} U^2(\pi) \frac{s_1^2 \sin^2[\delta(\mathbf{k}) + \delta(\mathbf{k}')] }{\chi_\perp \omega_b(\mathbf{q})} \frac{1}{Z} \frac{\text{sgn}[\nu - \varepsilon_+(\mathbf{k}')] }{[\omega_b(\mathbf{q}) + |\varepsilon_+(\mathbf{k}') - \nu|/Z]^3}. \end{aligned} \quad (46)$$

Likewise, taking a variation of (43b) yields a second linear equation per band,  $n = 1, 2$ . Adding and subtracting these as well yields two more linear relations in terms of even and odd variations with respect to half filling:

$$\begin{aligned} \nu \delta Z(+) + Z \delta\nu(+) &= (E - C)\delta\nu(+) + D \delta Z(+), \\ Z\mu_0 + \nu \delta Z(-) - Z\delta\nu(-) &= (E - C)\delta\nu(-) + D \delta Z(-). \end{aligned} \quad (47)$$

Here, we have constants

$$\begin{aligned}
C &= \frac{3}{2} \int \frac{d^2 k'}{(2\pi)^2} U^2(\pi) \frac{s_1^2}{\chi_\perp} \frac{\sin^2[\delta(\mathbf{k}) + \delta(\mathbf{k}')] }{\omega_b(\mathbf{q})} \frac{1}{Z} \frac{1}{[\omega_b(\mathbf{q}) + |\varepsilon_+(\mathbf{k}') - \nu|/Z]^2}, \\
D &= \frac{3}{2} \int \frac{d^2 k'}{(2\pi)^2} U^2(\pi) \frac{s_1^2}{\chi_\perp} \frac{\sin^2[\delta(\mathbf{k}) + \delta(\mathbf{k}')] }{\omega_b(\mathbf{q})} \frac{1}{Z} \frac{\text{sgn}[\nu - \varepsilon_+(\mathbf{k}')] |\varepsilon_+(\mathbf{k}') - \nu|/Z}{[\omega_b(\mathbf{q}) + |\varepsilon_+(\mathbf{k}') - \nu|/Z]^2},
\end{aligned} \tag{48}$$

and

$$E = \frac{3}{2} \int \frac{d^2 k'}{(2\pi)^2} U^2(\pi) \frac{s_1^2}{\chi_\perp} \frac{\sin^2[\delta(\mathbf{k}) + \delta(\mathbf{k}')] }{\omega_b(\mathbf{q})} \frac{2 \delta[\nu - \varepsilon_+(\mathbf{k}')] }{\omega_b(\mathbf{q}) + |\varepsilon_+(\mathbf{k}') - \nu|/Z}. \tag{49}$$

Collecting terms in (45) and in (47), we get

$$\delta Z(+)= -\frac{B}{F} \delta \nu(+)\quad \text{and}\quad \delta Z(+)= -\frac{2Z-E}{G} \delta \nu(+)\tag{50}$$

in the even channel, and we get

$$\delta Z(-)= \frac{B}{A} \delta \nu(-)\quad \text{and}\quad Z\mu_0 = E \delta \nu(-) - G \delta Z(-)\tag{51}$$

in the odd channel, where  $F = Z - A$  and  $G = \nu - D$ . These constants are then

$$F = \frac{3}{2} \int \frac{d^2 k'}{(2\pi)^2} U^2(\pi) \frac{s_1^2}{\chi_\perp} \frac{\sin^2[\delta(\mathbf{k}) + \delta(\mathbf{k}')] }{Z} \frac{1}{[\omega_b(\mathbf{q}) + |\varepsilon_+(\mathbf{k}') - \nu|/Z]^3}, \tag{52}$$

$$G = \frac{3}{2} \int \frac{d^2 k'}{(2\pi)^2} U^2(\pi) \frac{s_1^2}{\chi_\perp} \frac{\sin^2[\delta(\mathbf{k}) + \delta(\mathbf{k}')] }{Z} \frac{\text{sgn}[\nu - \varepsilon_+(\mathbf{k}')] }{[\omega_b(\mathbf{q}) + |\varepsilon_+(\mathbf{k}') - \nu|/Z]^2}. \tag{53}$$

In deriving expression (52), the first Eliashberg equation (43a) at half filling  $Z - 1 = C$  has been approximated by  $Z = C$ . This is exact at criticality,  $\Delta_b \rightarrow 0$ . And in deriving expression (53), the second Eliashberg equation (43b) for  $\nu$  at half filling has been applied.

We shall now evaluate the constants above that determine the linear response of the Eliashberg equations in the normal state driven by weak electron doping with respect to half filling: (43a) and (43b), as  $\mu_0 \rightarrow 0+$ . Criticality is again assumed at half filling:  $\Delta_b \rightarrow 0$ . Let us begin by evaluating the constant  $G$  (53). First, average it over the Fermi surface:  $G \rightarrow [D_+(\nu)]^{-1} (2\pi)^{-2} \int_{\text{BZ}} d^2 k G \delta[\varepsilon_+(\mathbf{k}) - \nu]$ . Second, replace the integrals over momentum with the product of  $\Omega$  and the spectral density (30) at half filling:  $U^2 F_0(\Omega) = \epsilon_E / \sqrt{\Omega^2 - \Delta_b^2}$  for  $\Omega > \Delta_b$ , and  $U^2 F_0(\Omega) = 0$  otherwise. This yields

$$G = \int_{\Delta_b}^{\omega_{\text{uv}}} d\Omega \frac{\epsilon_E}{\sqrt{\Omega^2 - \Delta_b^2}} \Omega \int_{-W_{\text{bottom}}}^{+W_{\text{top}}} d\varepsilon' Z^{-1} \frac{\text{sgn}(\nu - \varepsilon')}{[\Omega + |\varepsilon' - \nu|/Z]^2}. \tag{54}$$

Third, perform the first integral over the energy band  $\varepsilon_+(\mathbf{k})$  in the limit of strong on-site repulsion,  $U(\pi) \rightarrow \infty$ , in which case  $\nu$  approaches the top of the band,  $W_{\text{top}}$ . It is equal to

response/variation	$\delta Z$	$\delta\nu$
$\delta Z$	$A = \frac{\epsilon_E}{\Delta_b} - F$ with $F = \frac{1}{2} \frac{\epsilon_E}{\Delta_b} [\frac{\pi}{2} - I(y) - yI'(y)]$	$B = \frac{1}{2} \frac{\epsilon_E}{\Delta_b^2} [I'(y) - I'(0)]$
$\delta\nu$	$D = \nu - G$ with $G = \epsilon_E y I(y)$	$E = \pi \frac{\epsilon_E}{\Delta_b}$

TABLE III: Coefficients of the linear response to weak electron doping of the Eliashberg equations (43a) and (43b), at criticality  $\Delta_b \rightarrow 0$ : Eqs. (45) and (47). A closed form expression for the definite integral  $I(y)$  is given in Appendix C, where  $y = W/\epsilon_E$ .

$\Omega^{-1} - (W/Z + \Omega)^{-1}$ . Fourth, make the change of variable  $\Omega = \Delta_b \cosh(x)$  and take the limit  $\Delta_b \rightarrow 0$ . This yields  $G = \epsilon_E y I(y)$ , where  $I(y)$  is the definite integral (37a), with  $y = W/\epsilon_E$ . A closed-form expression for  $I(y)$  is obtained in Appendix C.

The remaining constants can be evaluated in a similar way. In particular, applying the same set of steps above to the expression for the constant  $F$  (52) yields the definite integral

$$F = \frac{1}{2} \frac{\epsilon_E}{\Delta_b} \int_0^\infty dx \frac{1}{\cosh x} \left[ 1 - \frac{1}{(1 + y \operatorname{sech} x)^2} \right] \quad (55)$$

at criticality,  $\Delta_b \rightarrow 0$ , where  $y = W/\epsilon_E$ . It is shown in Appendix C that (55) reduces to the closed-form expression  $F = \frac{1}{2} (\epsilon_E/\Delta_b) [\frac{\pi}{2} - I(y) - yI'(y)]$ , where  $I'(y)$  denotes the derivative of  $I(y)$ . Likewise, performing the same set of steps on the expression for the constant  $B$  (46) yields the definite integral

$$B = \frac{1}{2} \frac{\epsilon_E}{\Delta_b^2} \int_0^\infty dx \left[ \frac{1}{(\cosh x)^2} - \frac{1}{(y + \cosh x)^2} \right] \quad (56)$$

at criticality. Comparison with the definite integral (37a) therefore yields the expression  $B = \frac{1}{2} (\epsilon_E/\Delta_b^2) [I'(y) - I'(0)]$ . And recall that a closed-form expression for the constant  $A$  is obtained from that for  $F$  above through the identity  $A = Z - F$ . Last, performing the same set of steps on the expression for the constant  $E$  (49) yields the definite integral

$$E = 2 \frac{\epsilon_E}{\Delta_b} \int_0^\infty dx \frac{1}{\cosh x} = \pi \frac{\epsilon_E}{\Delta_b} \quad (57)$$

at criticality. This completes the evaluation of the constants that determine the linear response of the renormalized electronic structure shown in Fig. 4 to weak electron doping at criticality,  $\Delta_b \rightarrow 0$ .

In conclusion, at weak electron doping, the normal-state Eliashberg equations (43a) and (43b) yield independent linear-response equations in the even and in the odd channels, (50)

$W/W_{\text{top}}$	$\varepsilon_E/W$	$\epsilon_E/W$	$\chi_E$	$X_E W$
1.0	0.343	0.366	2.045	8.671
1.1	0.298	0.303	2.120	9.673
1.2	0.261	0.255	2.200	10.780
1.3	0.231	0.218	2.284	12.001
1.4	0.206	0.189	2.373	13.344
1.5	0.185	0.165	2.467	14.821

TABLE IV: Numerical solutions of Eliashberg equations at half filling, at criticality, in the limit  $U(\pi) \rightarrow \infty$ : Eq. (38). Also listed are the susceptibilities about half filling:  $\delta\mu_1 = \chi_E \mu_0 = \delta\mu_2$  and  $\delta Z_2/Z = X_E \mu_0 = -\delta Z_1/Z$ . Note that  $W/W_{\text{top}} = 1 + (t_1^{\parallel}/t_1^{\perp})$ .

and (51). The coefficients of the linear response are summarized by Table III. In the even channel, we thereby get  $\delta Z(+)=0$  and  $\delta\nu(+)=0$  if  $BG \neq (2Z - E)F$ . Notice that  $B$ ,  $G$  and  $F$  are positive, while  $2Z - E = (2\varepsilon_E - \pi\epsilon_E)/\Delta_b$  is negative by Table IV. The former inequality is therefore valid, and we get  $\delta Z_1 = -\delta Z_2$  and  $\delta\mu_1 = \delta\mu_2$ . And in the odd channel, (51) yields

$$\delta Z(-) = \chi_E \frac{B}{A} \mu_0 \quad \text{and} \quad \delta\nu(-) = \chi_E \mu_0, \quad (58)$$

with susceptibility  $\chi_E = Z/(E - \frac{BG}{A})$ . The latter can be calculated from the previous closed-form expressions for the constants  $A$  thru  $G$  that are listed in Table III, and the results are listed in Table IV. Importantly,  $\chi_E$  is positive at  $W/W_{\text{top}}$  between 1.0 and 1.5, which corresponds to at most weak eccentricity in the electron/hole Fermi surface pockets at the corner of the two-iron Brillouin zone. Recall that  $\delta\nu(-) = \frac{1}{2}(\delta\mu_1 + \delta\mu_2)$  is the average chemical-potential shift, which is equal to  $\delta\mu_1 = \delta\mu_2$ . The latter and (58) therefore imply a *rigid shift* of the renormalized electronic structure at half filling by a chemical-potential shift proportional to the electron doping. Figure 5 is such a rigid shift of Fig. 4. Also recall that  $\delta Z(-) = \frac{1}{2}(\delta Z_2 - \delta Z_1)$ , which is equal to  $\delta Z_2 = -\delta Z_1$ . Upon electron doping, the latter and (58) imply, on the other hand, that the wavefunction renormalization increases with respect to  $Z = \varepsilon_E/\Delta_b$  on the hole Fermi surface pockets ( $n = 2$ ), while that it decreases with respect to  $Z$  on the electron Fermi surface pockets ( $n = 1$ ). The magnitude of the equal and opposite variation in the wavefunction renormalization is best stated as  $\delta Z(-)/Z = X_E \mu_0$ , where  $X_E = \frac{B}{A}/(E - \frac{BG}{A})$ . The values of  $X_E W$  listed in Table IV suggest that  $Z_1 \approx 1$  and

that  $Z_2 \sim 2Z$  at electron doping greater than  $x_0$ . This will be discussed at length below and in the next section.

Yet what is the superconducting gap at weak electron doping with respect to half filling? Inspection of the gap equations in the Eliashberg equations (28) yields that they are equivalent to the ones *at* half filling to linear order in the variations  $\delta Z_1$ ,  $\delta Z_2$ ,  $\delta\mu_1$  and  $\delta\mu_2$ , and in the gaps  $\Delta_1$  and  $\Delta_2$ . Because  $\Delta_1$  and  $\Delta_2$  are null at half filling, the *linear* susceptibility of these quantities with electron doping  $\mu_0 > 0$  is also null. Any superconducting gap that opens at weak electron doping must therefore depend non-linearly on the doping concentration. (See Fig. 6.)

### C. Moderate Electron Doping

Let us next seek solutions to the Eliashberg equations, (29a-29c), at moderate electron doping  $x \sim x_0$ . The previous linear response due to weak electron doping predicts a rigid shift in energy of the renormalized electronic structure at half filling displayed by Fig. 4. It is depicted by Fig. 5, where the top of the bonding (+) band lies just above the Fermi level. The previous linear response about half filling also predicts wavefunction renormalizations  $Z_2$  and  $Z_1$  for the bonding band ( $n = 2$ ) and for the anti-bonding band ( $n = 1$ ), respectively, above and below the unique value at half filling. What then does the third Eliashberg equation for the superconducting gap (29c) predict at moderate doping?

We shall follow the historical approach for the solution of the Eliashberg equations in the case of the electron-phonon interaction<sup>44,45,51-54</sup>. In particular, before confronting the gap equation, it is useful first to obtain the wavefunction renormalizations of the two bands at the Fermi level in the normal state. Neglecting frequency dependence, the first Eliashberg equation (29a) then yields the following wavefunction renormalizations at the Fermi level,  $\omega = 0$ :

$$Z_n - 1 = \int_{\Delta_b}^{\omega_{uv}} d\Omega U^2 F_0^{(n,\bar{n})}(\Omega, \mu_n, \mu_{\bar{n}}) \left( \frac{1}{\Omega} - \frac{1}{W/Z_{\bar{n}} + \Omega} \right). \quad (59)$$

Again, the order of integration in (29a) has been reversed. Next, assume weak to moderate wavefunction renormalization in the anti-bonding (-) band and strong wavefunction renormalization in the bonding (+) band:  $\lambda_1$  such that  $W/Z_1 \gg \Delta_b$ , and  $\lambda_2 \gg 1$  such that  $W/Z_2 \ll \Delta_b$ . Here  $\lambda_n = Z_n - 1$ . Notice that the last inequality is consistent with the previous results at weak electron doping:  $\varepsilon_E/\Delta_b < Z_2$ . The above Eliashberg equations (59)

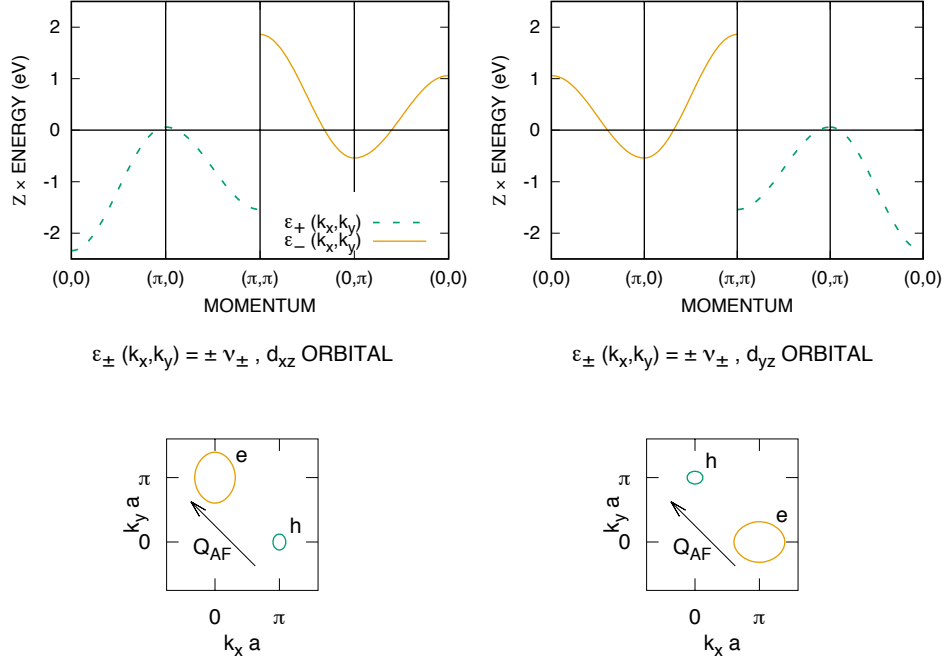


FIG. 5: Renormalized electron bands and Fermi surfaces at electron doping after the Lifshitz transition. Again, the orbital character is only approximate.

then yield the results

$$\lambda_2 \cong \int_{\Delta_b}^{\omega_{uv}} d\Omega \Omega^{-1} U^2 F_0^{(2,1)}(\Omega, \mu_2, \mu_1), \quad (60)$$

and

$$\lambda_1 \cong \frac{W}{Z_2} \int_{\Delta_b}^{\omega_{uv}} d\Omega \Omega^{-2} U^2 F_0^{(1,2)}(\Omega, \mu_1, \mu_2), \quad (61)$$

or  $\lambda_1 \cong (W/Z_2)\lambda_2 \overline{\Omega^{-1}}$ . The distribution in the average  $\overline{\Omega^{-1}}$  is normalized by the integral (60) because of the approximate identity  $U^2 F_0^{(1,2)}(\Omega, \mu_1, \mu_2) \cong U^2 F_0^{(2,1)}(\Omega, \mu_2, \mu_1)$ . By (30), the latter is due to the approximate identity obeyed by the density of states,  $D_-(\mu_1) \cong D_+(\mu_2)$ , at  $\mu_1$  and  $\mu_2$  near the bottom and near the top of the respective bands  $\varepsilon_-(\mathbf{k})$  and  $\varepsilon_+(\mathbf{k})$ . Here, also, we have applied the identity (44). Because  $\lambda_2 \gg 1$ , we then have that  $\lambda_1 \cong W \overline{\Omega^{-1}}$ . Finally, the initial assumption of moderate  $\lambda_1$  is confirmed by noting that  $W/Z_1 \cong W/(1 + W \overline{\Omega^{-1}}) \cong (\overline{\Omega^{-1}})^{-1}$ , which is much greater than  $\Delta_b$ .

We shall now show that an instability to  $S$ -wave Cooper pairing exists that alternates in sign between the strong electron-type Fermi surface of the anti-bonding ( $-$ ) band,  $n = 1$ , and

the weak hole-type Fermi surface of the bonding (+) band,  $n = 2$ . (See Fig. 5.) In particular, assume the simple BCS form (40) for the frequency dependence of the respective gaps,  $\Delta_1(\omega)$  and  $\Delta_2(\omega)$ , with frequency cutoffs  $\omega_c(1)$  and  $\omega_c(2)$ . After neglecting the frequency dependence of the wavefunction renormalizations, the gap equations (29c) then read

$$Z_n \Delta_n = -2 \int_{|\Delta_{\bar{n}}|}^{\omega_c(\bar{n})} dE' \frac{\Delta_{\bar{n}}}{\sqrt{E'^2 - \Delta_{\bar{n}}^2}} \int_{\Delta_b}^{\omega_{uv}} d\Omega U^2 F_0^{(n, \bar{n})}(\Omega; \mu_n, \mu_{\bar{n}}) \frac{1}{\Omega + E'}. \quad (62)$$

Assume, further, the BCS limit:  $\omega_c(1), \omega_c(2) \rightarrow 0$ . Taking the normal-state values for the wavefunction renormalizations discussed above is then valid. Also, the denominator above,  $\Omega + E'$ , can then be replaced by  $\Omega$ . After comparison with (60), we thereby arrive at the gap equations

$$Z_n \Delta_n = -2 \int_{|\Delta_{\bar{n}}|}^{\omega_c(\bar{n})} dE' \frac{\lambda_2}{\sqrt{E'^2 - \Delta_{\bar{n}}^2}} \Delta_{\bar{n}}, \quad (63)$$

or  $\Delta_1 = -K_{1,2} \Delta_2$  and  $\Delta_2 = -K_{2,1} \Delta_1$ , with kernels

$$K_{1,2} = 2 \frac{\lambda_2}{Z_1} \sinh^{-1} \left[ \frac{\sqrt{\omega_c^2(2) - \Delta_2^2}}{|\Delta_2|} \right] \quad \text{and} \\ K_{2,1} = 2 \frac{\lambda_2}{Z_2} \sinh^{-1} \left[ \frac{\sqrt{\omega_c^2(1) - \Delta_1^2}}{|\Delta_1|} \right]. \quad (64)$$

Importantly, these equations imply that  $\Delta_1$  and  $\Delta_2$  are of opposite sign! An  $S^{+-}$  pairing instability therefore exists between the strong and the weak Fermi surfaces shown in Fig. 5.

To obtain explicit solutions of the gap equations, it is useful to multiply and divide these, which yields

$$1 = K_{1,2} K_{2,1} \quad \text{and} \quad \left( \frac{\Delta_2}{\Delta_1} \right)^2 = \frac{K_{2,1}}{K_{1,2}}. \quad (65)$$

Taking the product of the above then gives  $|\Delta_2/\Delta_1| = K_{2,1} \cong 2 \sinh^{-1}[\sqrt{\omega_c^2(1) - \Delta_1^2}/|\Delta_1|]$ . Assuming  $|\Delta_1|$  near  $\omega_c(1)$  in turn yields  $|\Delta_2| \cong 2\sqrt{2\omega_c(1)}\sqrt{\omega_c(1) - |\Delta_1|}$ . Substituting the previous into the first gap equation displayed by (65) then yields

$$1 \cong 2 \frac{\lambda_2}{Z_1 \omega_c(1)} \sinh^{-1} \left[ \frac{\omega_c(2)}{|\Delta_2|} \right], \quad (66)$$

or  $|\Delta_2| \sim (Z_1/Z_2)\omega_c(1)$ . This solution thereby confirms the instability of the Fermi surfaces to  $S^{+-}$  pairing, where the wavefunction renormalization  $Z_1$  on the larger electron-type Fermi surface is of moderate size compared to unity, while the wavefunction renormalization  $Z_2$  on the smaller hole-type Fermi surface is large compared to unity. (See Fig. 5.)

## V. DISCUSSION

The previous results of electron Fermi surface pockets and faint hole Fermi surface pockets at the corner of the folded (two-iron) Brillouin zone, with  $S^{+-}$  Cooper pairing that alternates in sign between them, is compared below to a local-moment model for electron-doped iron selenide and to high-temperature iron-selenide superconductors themselves.

### A. Comparison with Local-Moment Model

A local-moment model of the electronic physics in electron-doped iron selenide exists that captures some of the principal features of the above Eliashberg theory<sup>34</sup>. It contains a two-orbital Hund-Heisenberg Hamiltonian<sup>40</sup>, with intra-orbital ( $\parallel$ ) and inter-orbital ( $\perp$ ) Heisenberg exchange coupling constants that are positive, and that satisfy  $J_1^\parallel > J_1^\perp$  and  $J_2^\parallel = J_2^\perp$ . [See Appendix A, Eq. (A1).] It also contains Hund's Rule exchange coupling between the orbitals, with a ferromagnetic coupling constant,  $J_0 < 0$ . Importantly, the infinite- $U_0$  limit is taken, which means that the formation of spin singlets per site, per  $d\pm$  orbital, is suppressed. Electron hopping via the Hamiltonian  $H_{\text{hop}}$  (1) is also added at electron doping, but in the infinite- $U_0$  limit. Last, notice that orbital swap,  $d- \leftrightarrow d+$ , is a global symmetry of the Hund-Heisenberg Hamiltonian (A1). It is therefore most natural to consider the case where orbital swap  $P_{d,\bar{d}}$  is a global symmetry of the hopping Hamiltonian  $H_{\text{hop}}$  (1) as well. This requires the absence of mixing between the  $3d_{xz}$  and  $3d_{yz}$  orbitals:  $t_2^\perp = 0$ . The latter restriction for the validity of the two-orbital  $t$ - $J$  model emerges from the underlying extended Hubbard model in the large- $U_0$  limit at half filling<sup>31</sup>. (See Appendix A.) In such case, for example, the transverse spin susceptibilities of both models,  $\chi_\perp$ , coincide only in the limit  $t_2^\perp/i \rightarrow 0$ .

The author exploited the Schwinger-boson-slave-fermion representation of the correlated electron to study the above local-moment model<sup>34</sup>. In particular, the creation operator of the correlated electron is written as  $\tilde{c}_{i,\alpha,s}^\dagger = b_{i,\alpha,s}^\dagger f_{i,\alpha}^\dagger$ , along with the constraint per site-orbital

$$b_{i,\alpha,\uparrow}^\dagger b_{i,\alpha,\uparrow} + b_{i,\alpha,\downarrow}^\dagger b_{i,\alpha,\downarrow} + f_{i,\alpha}^\dagger f_{i,\alpha} = 2s_0. \quad (67)$$

Here,  $b_{i,\alpha,s}^\dagger$  and  $b_{i,\alpha,s}$  are creation and annihilation operators for Schwinger bosons,  $f_{i,\alpha}^\dagger$  and  $f_{i,\alpha}$  are the corresponding operators for the slave fermions, and  $s_0 = 1/2$  is the electron spin. The constraint (67) is enforced only on average over the bulk within mean field theory for

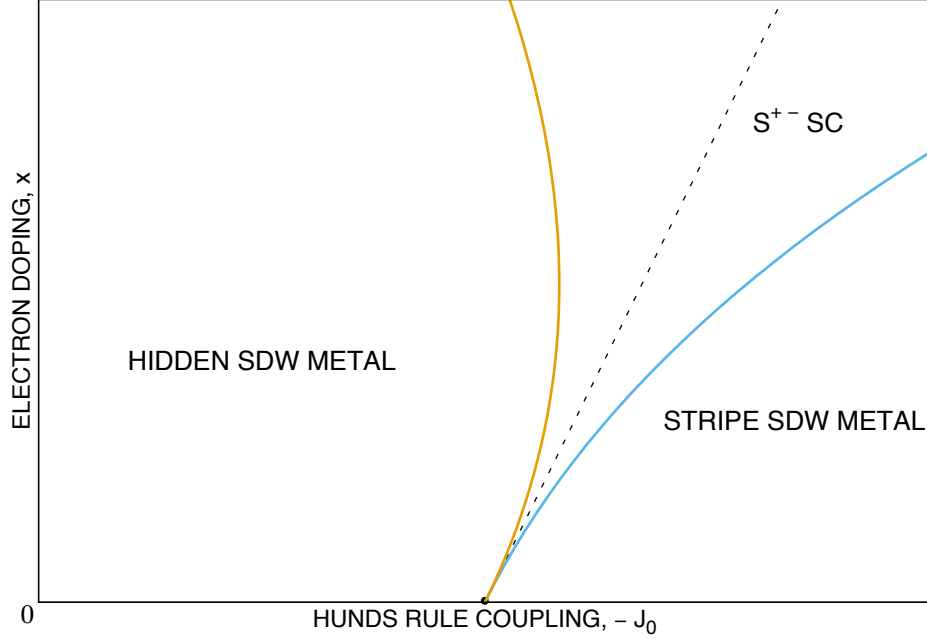


FIG. 6: Proposed phase diagram for local-moment model of electron-doped iron selenide (ref.<sup>34</sup>). The latter predicts the phase boundary approaching half filling (dashed line), which separates the hSDW state from the stripe SDW state. The intervening  $S^{+-}$  superconducting phase is predicted by the Eliashberg Theory introduced in the main text.

the hSDW state. In such case, a quantum-critical point exists at moderate Hund's Rule coupling  $-J_{0c}$ , where the spin-excitation spectrum collapses to zero energy at stripe SDW wave numbers  $(\pi/a, 0)$  and  $(0, \pi/a)$ . Specifically, the QCP occurs at<sup>34,40</sup>

$$-J_{0c} = 2(J_1^{\parallel} - J_1^{\perp}) + 2t_1^{\perp}x/(1-x)^2s_0 - 4J_2^{\parallel},$$

where  $x$  denotes the concentration of electron doping from half filling. It is depicted by the dashed line in Fig. 6. It is possible to identify the critical normal state of the previous Eliashberg theory at half filling ( $\Delta_b, \Delta_1, \text{ and } \Delta_2 \rightarrow 0$ ) with this QCP.

Both Schwinger-boson-slave-fermion mean field theory about the hidden Néel state and exact calculations on finite clusters for the above local-moment model find evidence for a  $d_{xz}$  and a  $d_{yz}$  Fermi-surface pocket at the corner of the two-iron Brillouin zone, at electron doping<sup>34</sup>. How then does the area of such electron-type Fermi-surface pockets compare with

that predicted by the previous Eliashberg theory, Fig. 5 ? Because the slave fermions do not carry spin, we have by charge conservation that

$$[D_+(\text{top}) + D_-(\text{bottom})]\delta\mu = 2[D_+(0) + D_-(0)]\mu_0. \quad (68)$$

The left-hand and the right-hand sides above correspond, respectively, to the cases where interactions are turned on (Fig. 4) and turned off (Fig. 1). In the above Eliashberg theory, (29a)-(29c) and (30), it has been assumed throughout that  $D_+(\varepsilon) \cong D_+(\text{top})$  and that  $D_-(\varepsilon) \cong D_-(\text{bottom})$ , however. Within that approximation, (68) thereby yields the susceptibility

$$\chi_E = \frac{\delta\mu}{\mu_0} \cong 2$$

from the Schwinger-boson-slave-fermion mean field theory. It agrees with the corresponding result from Eliashberg theory listed in Table IV, at hopping matrix element  $t_1^{\parallel} \rightarrow 0+$ , in which case the renormalized Fermi-surface pockets become perfectly circular as  $U_0$  grows large ( $x_0 \rightarrow 0$ ). This coincides with the hopping parameters studied in the local-moment model within the mean-field approximation<sup>34</sup>, in which case only  $t_1^{\perp}$  is non-zero.

And how do the predictions for wavefunction renormalization by the previous Eliashberg theory compare with the local-moment model<sup>34</sup>? A faint hole band with quasi-particle weight  $1/Z_2$  that vanishes at criticality,  $\Delta_b \rightarrow 0$ , is predicted by Eliashberg theory. (See Fig. 5.) It crosses the Fermi level near the corner of the folded (two-iron) Brillouin zone. At electron doping, both mean field theory and exact calculations on finite clusters find *no* evidence for hole excitations of this type in the two-orbital  $t$ - $J$  model at momenta  $(\pi/a, 0)$  and  $(0, \pi/a)$ . This is consistent with the previous. Also, in the large- $s_0$  limit, Schwinger-boson-slave-fermion mean field theory yields a coherent contribution to the one-particle Greens function equal to  $G_{\text{coh}}(\mathbf{k}, \omega) = s_0/[\omega + \mu_1 - \varepsilon_-(\mathbf{k})]$ . This is also consistent with the appreciable quasi-particle weight  $1/Z_1$  predicted by Eliashberg theory for the electron-type bands at the corner of the two-iron Brillouin zone.

Last, exact calculations of the local-moment model for electron-doped FeSe on finite clusters find evidence for an  $S$ -wave Cooper pair at an energy below a continuum of states near the QCP<sup>34</sup>. This is consistent with the prediction made above by Eliashberg theory of an instability of the Fermi surface to  $S^{+-}$  superconductivity. The former exact calculations also find a  $D$ -wave Cooper pair at an energy below the continuum of states, but at higher

energy than the  $S$ -wave Cooper pair. The separation in energy between the two pair states collapses to zero at the QCP.

## B. Comparison with Experiment

The prediction displayed by Fig. 5 of electron-type Fermi surface pockets centered at the corner of the two-iron Brillouin zone agrees with ARPES on electron-doped iron selenide<sup>1,9,14</sup>. Eliashberg theory also predicts the opening of an  $S$ -wave gap over such Fermi surface pockets, which agrees with ARPES on these systems<sup>2,10,11,13</sup>, as well as with STM<sup>5,12,15</sup>. Electron-electron interactions are expected to be moderately strong in iron selenide. This rules out conventional  $S$ -wave pairing over the electron Fermi surface pockets in electron-doped iron selenide. The  $S^{+-}$  Cooper pairing that is predicted here between the electron Fermi surface pockets and faint hole Fermi surface pockets at the corner of the folded Brillouin zone therefore potentially resolves the puzzling observations of isotropic pair gaps in electron-doped iron selenide.

The spectrum of hidden spin fluctuations centered at the antiferromagnetic wave number  $\mathbf{Q}_{\text{AF}} = (\pi/a, \pi/a)$  is what binds together electrons into  $S^{+-}$  Cooper pairs in the present Eliashberg theory. Recent inelastic neutron scattering studies on intercalated iron selenide<sup>55</sup> find low-energy magnetic excitations at wave numbers *around*  $\mathbf{Q}_{\text{AF}}$ , but no low-energy spin excitations *at*  $\mathbf{Q}_{\text{AF}}$ . Such a ring of low-energy magnetic excitations is in fact consistent with the low-energy hidden spin fluctuations that are exploited by the present Eliashberg theory. In particular, both the two-orbital local-moment model discussed above and the underlying extended Hubbard model for electron-doped iron selenide mentioned previously find that the low-energy hidden spin fluctuations centered at  $\mathbf{Q}_{\text{AF}}$  are not observable in the true-spin channel of the iron atoms<sup>31,41</sup>. This leaves a ring of observable spin excitations around the antiferromagnetic wavevector  $\mathbf{Q}_{\text{AF}}$ , in agreement with inelastic neutron scattering<sup>55</sup>.

Although the present study suggests that the iron  $3d_{xz}/3d_{yz}$  orbitals are the principal ones in electron-doped iron selenide, ARPES and density-functional theory indicate that the iron  $3d_{xy}$  orbital also plays an important role<sup>56</sup>. A relatively flat and hole-type  $3d_{xy}$  band<sup>25,57</sup> can be added to the present Eliashberg Theory (Fig. 3) for  $3d_{xz}/3d_{yz}$  electrons interacting with hidden spin fluctuations<sup>58</sup>. Because electrons in the  $3d_{xy}$  band do *not* interact with hidden spin fluctuations, they may be considered to be spectators. Weak

mixing of the two  $3d_{xz}/3d_{yz}$  bands with the  $3d_{xy}$  band results in the expected level repulsion of the renormalized electron/hole Fermi surface pockets shown in Fig. 4. (See ref.<sup>58</sup>, Fig. S3.) This implies that the Lifshitz transition to such a renormalized band structure at half filling is robust in the presence of weak mixing with the  $3d_{xy}$  band. Also, within the present Eliashberg Theory, a direct calculation of the propagator for such  $3d_{xy}$  spectator electrons finds that they inherit divergent wavefunction renormalization at the Fermi level from the  $3d_{xz}/3d_{yz}$  electrons at half filling. (See ref.<sup>58</sup>, Eq. (S20).) In particular, the vanishing quasi-particle weight of the  $3d_{xz}/3d_{yz}$  electrons at the Fermi level,  $Z^{-1} \rightarrow 0$ , implies the vanishing quasi-particle weight of the  $3d_{xy}$  electrons at the Fermi level. Similar results are obtained when the spin-orbit interaction is included on iron atoms that are strictly equivalent over the square lattice<sup>58</sup>. Last, the tips of the electron Fermi surface pockets ( $n = 1$ ) shown in Fig. 4 can acquire  $3d_{xy}$  orbital character if the electron/hole Fermi surface pockets are large enough. This coincides with predictions made by band-structure calculations on alkali-atom intercalated iron selenides<sup>22,24</sup>.

## VI. CONCLUSIONS

We have shown above how low-energy hidden spin fluctuations in electron-doped iron selenide near the checkerboard wavevector for the square lattice of iron atoms lead to superconductivity, with isotropic Cooper pairs that alternate in sign between strong electron Fermi surface pockets and faint hole Fermi surface pockets. Both Fermi surface pockets lie at the corner of the folded (two-iron) Brillouin zone. Like true spin fluctuations in the case of iron-pnictide materials, the hidden spin fluctuations are due to nested Fermi surfaces. However, unlike true spin fluctuations, the exchange of hidden spin fluctuations can give rise to significant band shifts. In particular, Eliashberg theory reveals that they incite a Lifshitz transition from nested Fermi surfaces at the center and at the corner of the unfolded (one-iron) Brillouin zone to nested Fermi surfaces at the corner of the folded Brillouin zone<sup>31</sup>. Also, like true spin fluctuations in the case of iron-pnictide materials<sup>48-50,59-61</sup>, hidden spin fluctuations give rise to repulsive inter-band interactions between electrons that favor  $S^{+-}$  Cooper pairing between the renormalized Fermi surface pockets. Unlike true spin fluctuations, however, orbital matrix elements result in weak effective interactions due to hidden spin fluctuations at strong Hubbard repulsion. This justifies the neglect of vertex corrections

in Eliashberg theory<sup>44,45</sup>.

It has also been recently argued by the author that hidden spin fluctuations account for the ring of low-energy spin excitations at the checkerboard wavevector observed by inelastic neutron scattering in electron-doped iron selenide<sup>41,55</sup>. This, coupled with the prediction of  $S^{+-}$  superconductivity mentioned above, suggests that hidden spin fluctuations play an important role in high-temperature iron-selenide superconductors.

### **Acknowledgments**

The author is indebted to Stefan-Ludwig Drechsler for suggesting that an Eliashberg theory in both the particle-hole and in the particle-particle channels is possible. (Cf. ref.<sup>53</sup>, Chapter 5.) He also thanks Yongtao Cui for useful discussions. This work was supported in part by the US Air Force Office of Scientific Research under grant no. FA9550-17-1-0312.

## Appendix A: Two-Orbital Hund-Heisenberg Model and Extended Hubbard Model

The two-orbital Heisenberg model over the square lattice that includes Hund's Rule coupling is defined by the Hamiltonian<sup>40</sup>

$$H = \sum_i J_0 \mathbf{S}_{i,d-} \cdot \mathbf{S}_{i,d+} + \sum_{\langle i,j \rangle} \sum_{\alpha} (J_1^{\parallel} \mathbf{S}_{i,\alpha} \cdot \mathbf{S}_{j,\alpha} + J_1^{\perp} \mathbf{S}_{i,\alpha} \cdot \mathbf{S}_{j,\bar{\alpha}}) + \sum_{\langle\langle i,j \rangle\rangle} \sum_{\alpha} (J_2^{\parallel} \mathbf{S}_{i,\alpha} \cdot \mathbf{S}_{j,\alpha} + J_2^{\perp} \mathbf{S}_{i,\alpha} \cdot \mathbf{S}_{j,\bar{\alpha}}), \quad (\text{A1})$$

where  $\alpha = d-$  or  $d+$ . The hidden order Néel antiferromagnetic is stable at sufficiently weak Hund's Rule coupling  $-J_0$  when  $J_1^{\parallel} > J_1^{\perp}$ . In the limit of large spin<sup>40</sup>,  $s_0 \rightarrow \infty$ , it has spin rigidity

$$\rho_s = 2s_0^2 [J_1^{\parallel} - J_1^{\perp} + 2(J_2^{\perp} - J_2^{\parallel})] \quad (\text{A2})$$

and a transverse spin susceptibility

$$\chi_{\perp} = a^{-2} (J_0 + 4J_1^{\parallel} + 4J_2^{\perp})^{-1}. \quad (\text{A3})$$

The dynamical susceptibility for hidden spin fluctuations  $\mathbf{S}_{i,d+} - \mathbf{S}_{i,d-}$  can also be calculated<sup>40</sup> at large  $s_0$ . At the long-wavelength limit,  $\mathbf{q} \rightarrow \mathbf{Q}_{\text{AF}}$ , minus it yields the universal form given in the text for the propagator  $D(\mathbf{q}, \omega)$  [Eqs. (8) and (9)], with spin  $s_1 = s_0$ , and with a null spin gap,  $\Delta_b = 0$ .

The Hamiltonian of the underlying extended Hubbard model<sup>31</sup> has three parts:  $H = H_{\text{hop}} + H_U + H_{\text{sprx}}$ . On-site Coulomb repulsion is counted by the second term<sup>62</sup>,

$$H_U = \sum_i [U_0 n_{i,\alpha,\uparrow} n_{i,\alpha,\downarrow} + J_0 \mathbf{S}_{i,d-} \cdot \mathbf{S}_{i,d+} + U'_0 n_{i,d+} n_{i,d-} + J'_0 (c_{i,d+,\uparrow}^{\dagger} c_{i,d+,\downarrow}^{\dagger} c_{i,d-,\downarrow} c_{i,d-,\uparrow} + \text{h.c.})]. \quad (\text{A4})$$

where  $n_{i,\alpha,s}$  is the occupation operator, and where  $n_{i,\alpha} = n_{i,\alpha,\uparrow} + n_{i,\alpha,\downarrow}$ . Above,  $U_0 > 0$  is the intra-orbital on-site Coulomb repulsion energy, while  $U'_0 > 0$  is the inter-orbital one. Also,  $J'_0$  is the matrix element for on-site-orbital Josephson tunneling. The third and last term in the Hamiltonian represents super-exchange interactions among the iron spins via the selenium atoms:

$$H_{\text{sprx}} = \sum_{\langle i,j \rangle} J_1^{(\text{sprx})} (\mathbf{S}_{i,d-} + \mathbf{S}_{i,d+}) \cdot (\mathbf{S}_{j,d-} + \mathbf{S}_{j,d+}) + \sum_{\langle\langle i,j \rangle\rangle} J_2^{(\text{sprx})} (\mathbf{S}_{i,d-} + \mathbf{S}_{i,d+}) \cdot (\mathbf{S}_{j,d-} + \mathbf{S}_{j,d+}). \quad (\text{A5})$$

Above,  $J_1^{(\text{sprx})}$  and  $J_2^{(\text{sprx})}$  are positive super-exchange coupling constants over nearest neighbor and next-nearest neighbor iron sites.

## Appendix B: Orbital Matrix Element

The operators that create the eigenstates (5) of the electron hopping Hamiltonian,  $H_{\text{hop}}$ , are

$$c_s^\dagger(n, \mathbf{k}) = \mathcal{N}^{-1/2} \sum_i \sum_{\alpha=0,1} (-1)^{\alpha n} e^{i(2\alpha-1)\delta(\mathbf{k})} e^{i\mathbf{k}\cdot\mathbf{r}_i} c_{i,\alpha,s}^\dagger, \quad (\text{B1})$$

where  $\alpha = 0$  and  $1$  index the  $d-$  and  $d+$  orbitals, and where  $n = 1$  and  $2$  index the anti-bonding and bonding orbitals  $(-i)d_{y(\delta)z}$  and  $d_{x(\delta)z}$ . The inverse of the above is then

$$c_{i,\alpha,s}^\dagger = \mathcal{N}^{-1/2} \sum_{\mathbf{k}} \sum_{n=1,2} (-1)^{\alpha n} e^{-i(2\alpha-1)\delta(\mathbf{k})} e^{-i\mathbf{k}\cdot\mathbf{r}_i} c_s^\dagger(n, \mathbf{k}). \quad (\text{B2})$$

Plugging (B2) and its hermitian conjugate into the expression for the hidden electron spin operator,

$$\mathbf{S}(\pi, \mathbf{q}) = \frac{1}{2} \sum_s \sum_{s'} \sum_i \sum_{\alpha} (-1)^\alpha e^{i\mathbf{q}\cdot\mathbf{r}_i} \frac{1}{2} c_{i,\alpha,s}^\dagger \boldsymbol{\sigma}_{s,s'} c_{i,\alpha,s'}, \quad (\text{B3})$$

yields the form

$$\mathbf{S}(\pi, \mathbf{q}) = \frac{1}{2} \sum_s \sum_{s'} \sum_{\mathbf{k}} \sum_{n,n'} \mathcal{M}_{n,\mathbf{k};n',\mathbf{k}'} c_s^\dagger(n', \mathbf{k}') \boldsymbol{\sigma}_{s,s'} c_{s'}(n, \mathbf{k}), \quad (\text{B4})$$

with the matrix element<sup>31</sup>

$$\mathcal{M}_{n,\mathbf{k};n',\mathbf{k}'} = \begin{cases} -i \sin[\delta(\mathbf{k}) - \delta(\mathbf{k}')] & \text{for } n' = n, \\ \cos[\delta(\mathbf{k}) - \delta(\mathbf{k}')] & \text{for } n' \neq n. \end{cases} \quad (\text{B5})$$

Here,  $\mathbf{k}' = \mathbf{k} - \mathbf{q}$ . Now replace  $\mathbf{k}'$  above with  $\bar{\mathbf{k}}' = \mathbf{k}' + \mathbf{Q}_{\text{AF}}$ . Using the identity

$$\delta(\mathbf{k}' + \mathbf{Q}_{\text{AF}}) = \pm \frac{\pi}{2} - \delta(\mathbf{k}') \quad (\text{B6})$$

yields the equivalent expression<sup>31</sup>

$$\mathcal{M}_{n,\mathbf{k};n',\bar{\mathbf{k}}'} = \begin{cases} \pm i \cos[\delta(\mathbf{k}) + \delta(\mathbf{k}')] & \text{for } n' = n, \\ \pm \sin[\delta(\mathbf{k}) + \delta(\mathbf{k}')] & \text{for } n' \neq n. \end{cases} \quad (\text{B7})$$

Here,  $\mathbf{k}' = \mathbf{k} - \mathbf{q} - \mathbf{Q}_{\text{AF}}$ .

### Appendix C: Definite Integrals Approaching Criticality

The following definite integrals appear in the solution of the Eliashberg equations (36) at half filling, at criticality:

$$I(y) = \int_0^\infty dx \frac{1}{y + \cosh x}, \quad (\text{C1})$$

and

$$J(y) = \int_0^\infty dx \ln \left( 1 + \frac{y}{\cosh x} \right). \quad (\text{C2})$$

The first one (C1) can be evaluated directly by using the definition  $\cosh x = \frac{1}{2}z + \frac{1}{2}z^{-1}$ , with  $z = e^x$ . Changing variables leads to the expression

$$I(y) = \int_1^\infty dz \frac{2}{z^2 + 2yz + 1}. \quad (\text{C3})$$

Factorizing the denominator into  $(z - z_+)(z - z_-)$ , with  $z_\pm = -y \pm \sqrt{y^2 - 1}$ , and resolving the integrand into partial fractions yields

$$I(y) = \int_1^\infty dz \frac{1}{z_+ - z_-} \left( \frac{1}{z - z_+} - \frac{1}{z - z_-} \right). \quad (\text{C4})$$

Hence, we arrive at the closed-form expression

$$I(y) = \frac{1}{\sqrt{y^2 - 1}} \ln \left( \frac{1 + y + \sqrt{y^2 - 1}}{1 + y - \sqrt{y^2 - 1}} \right). \quad (\text{C5})$$

Simplifying the argument of the logarithm above yields the equivalent expression

$$I(y) = \frac{1}{\sqrt{y^2 - 1}} \ln \left( \frac{1}{y - \sqrt{y^2 - 1}} \right). \quad (\text{C6})$$

And concerning the second definite integral (C2), notice that (i)  $dJ/dy = I$  and (ii)  $J(0) = 0$ .

The expression

$$J(y) = \frac{\pi^2}{8} + \frac{1}{2} [\ln(y - \sqrt{y^2 - 1})]^2 \quad (\text{C7})$$

satisfies both conditions. It therefore coincides with the definite integral (C2).

Further, the constant  $F$  that appears in the linear response at half filling to electron doping can also be evaluated in closed form. Expression (55) for it can be re-expressed as

$$F = \lim_{\Delta_b \rightarrow 0} \frac{1}{2} \frac{\epsilon_E}{\Delta_b} \left[ \int_0^{x_2} dx \operatorname{sech} x + \frac{\partial}{\partial y} \int_0^{x_2} dx (1 + y \operatorname{sech} x)^{-1} \right], \quad (\text{C8})$$

where  $x_2 = \cosh^{-1}(\omega_{uv}/\Delta_b)$ . But  $(1 + y \operatorname{sech} x)^{-1} = 1 - y(y + \cosh x)^{-1}$ , which yields the identity

$$\int_0^{x_2} dx (1 + y \operatorname{sech} x)^{-1} = x_2 - y \int_0^{x_2} dx (y + \cosh x)^{-1}.$$

Substituting it above then yields the closed-form expression

$$F = \frac{1}{2} \frac{\epsilon_E}{\Delta_b} \left[ \frac{\pi}{2} - I(y) - yI'(y) \right] \quad (\text{C9})$$

as  $\Delta_b \rightarrow 0$ , where  $I'(y)$  is the derivative of (C6).

- 
- <sup>1</sup> T. Qian, X.-P. Wang, W.-C. Jin, P. Zhang, P. Richard, G. Xu, X. Dai, Z. Fang, J.-G. Guo, X.-L. Chen, H. Ding, “Absence of a Holelike Fermi Surface for the Iron-Based  $K_{0.8}Fe_{1.7}Se_2$  Superconductor Revealed by Angle-Resolved Photoemission Spectroscopy”, *Phys. Rev. Lett.* **106**, 187001 (2011).
- <sup>2</sup> M. Xu, Q. Q. Ge, R. Peng, Z. R. Ye, Juan Jiang, F. Chen, X. P. Shen, B. P. Xie, Y. Zhang, A. F. Wang, X. F. Wang, X. H. Chen, and D. L. Feng, “Evidence for an S-Wave Superconducting Gap in  $K_xFe_{2-y}Se_2$  from Angle-Resolved Photoemission”, *Phys. Rev. B* **85**, 220504(R) (2012).
- <sup>3</sup> B. Zeng, B. Shen, G. F. Chen, J. B. He, D. M. Wang, C. H. Li, and H. H. Wen, “Nodeless Superconductivity of Single-Crystalline  $K_xFe_{2-y}Se_2$  Revealed by the Low-Temperature Specific Heat”, *Phys. Rev. B* **83**, 144511 (2011).
- <sup>4</sup> Weiqiang Yu, L. Ma, J. B. He, D. M. Wang, T.-L. Xia, G. F. Chen, and Wei Bao, “ $^{77}Se$  NMR Study of the Pairing Symmetry and the Spin Dynamics in  $K_yFe_{2-x}Se_2$ ”, *Phys. Rev. Lett.* **106**, 197001 (2011).
- <sup>5</sup> Q.-Y. Wang, Z. Li, W.-H. Zhang, Z.-C. Zhang, J.-S. Zhang, W. Li, H. Ding, Y.-B. Ou, P. Deng, K. Chang, J. Wen, C.-L. Song, K. He, J.-F. Jia, S.-H. Ji, Y. Wang, L. Wang, X. Chen, X. Ma, Q.-K. Xue, “Interface-Induced High-Temperature Superconductivity in Single Unit-Cell FeSe Films on  $SrTiO_3$ ”, *Chin. Phys. Lett.* **29**, 037402 (2012).
- <sup>6</sup> W.-H. Zhang, Y. Sun, J.-S. Zhang, F.-S. Li, M.-H. Guo, Y.-F. Zhao, H.-M. Zhang, J.-P. Peng, Y. Xing, H.-C. Wang, T. Fujita, A. Hirata, Z. Li, H. Ding, C.-J. Tang, M. Wang, Q.-Y. Wang, K. He, S.-H. Ji, X. Chen, J.-F. Wang, Z.-C. Xia, L. Li, Y.-Y. Wang, J. Wang, L.-L. Wang, M.-W. Chen, Q.-K. Xue, and X.-C. Ma, “Direct Observation of High-Temperature Superconductivity in One-Unit-Cell FeSe Films”, *Chin. Phys. Lett.* **31**, 017401 (2014).
- <sup>7</sup> L.Z. Deng, B. Lv, Z. Wu, Y.Y. Xue, W.H. Zhang, F.S. Li, L.L. Wang, X.C. Ma, Q.K. Xue, and C.W. Chu, “Meissner and Mesoscopic Superconducting States in 1–4 Unit-Cell FeSe Films”, *Phys. Rev. B* **90**, 214513 (2014).
- <sup>8</sup> J.-F. Ge, Z.-L. Liu, C. Liu, C.-L. Gao, D. Qian, Q.-K. Xue, Y. Liu, J.-F. Jia, “Superconductivity Above 100 K in Single-Layer FeSe Films on Doped  $SrTiO_3$ ”, *Nat. Mater.* **14**, 285 (2015).
- <sup>9</sup> D. Liu, W. Zhang, D. Mou, J. He, Y.-B. Ou, Q.-Y. Wang, Z. Li, L. Wang, L. Zhao, S. He, Y. Peng, X. Liu, C. Chaoyu, L. Yu, G. Liu, X. Dong, J. Zhang, C. Chen, Z. Xu, J. Hu, X. Chen,

- Z. Ma, Q. Xue and X.J. Zhou, “Electronic Origin of High-Temperature Superconductivity in Single-Layer FeSe Superconductor”, *Nat. Comm.* **3**, 931 (2012).
- <sup>10</sup> R. Peng, X.P. Shen, X. Xie, H.C. Xu, S.Y. Tan, M. Xia, T. Zhang, H.Y. Cao, X.G. Gong, J.P. Hu, B.P. Xie, D. L. Feng, “Measurement of an Enhanced Superconducting Phase and a Pronounced Anisotropy of the Energy Gap of a Strained FeSe Single Layer in FeSe/Nb: SrTiO<sub>3</sub>/KTaO<sub>3</sub> Heterostructures Using Photoemission Spectroscopy”, *Phys. Rev. Lett.* **112**, 107001 (2014).
- <sup>11</sup> J.J. Lee, F.T. Schmitt, R.G. Moore, S. Johnston, Y.-T. Cui, W. Li, M. Yi, Z.K. Liu, M. Hashimoto, Y. Zhang, D.H. Lu, T.P. Devereaux, D.-H. Lee and Z.-X. Shen, “Interfacial Mode Coupling as the Origin of the Enhancement of  $T_c$  in FeSe Films on SrTiO<sub>3</sub>”, *Nature* **515**, 245 (2014).
- <sup>12</sup> Q. Fan, W.H. Zhang, X. Liu, Y.J. Yan, M.Q. Ren, R. Peng, H.C. Xu, B.P. Xie, J.P. Hu, T. Zhang, and D.L. Feng, “Plain S-Wave Superconductivity in Single-Layer FeSe on SrTiO<sub>3</sub> Probed by Scanning Tunneling Microscopy”, *Nat. Phys.* **11**, 946 (2015).
- <sup>13</sup> L. Zhao, A. Liang, D. Yuan, Y. Hu, D. Liu, J. Huang, S. He, B. Shen, Y. Xu, X. Liu, L. Yu, G. Liu, H. Zhou, Y. Huang, X. Dong, F. Zhou, Z. Zhao, C. Chen, Z. Xu, X.J. Zhou, “Common Electronic Origin of Superconductivity in (Li,Fe)OHFeSe Bulk Superconductor and Single-Layer FeSe/SrTiO<sub>3</sub> Films”, *Nat. Comm.* **7**, 10608 (2016).
- <sup>14</sup> X.H. Niu, R. Peng, H.C. Xu, Y.J. Yan, J. Jiang, D.F. Xu, T.L. Yu, Q. Song, Z.C. Huang, Y.X. Wang, B.P. Xie, X.F. Lu, N.Z. Wang, X.H. Chen, Z. Sun, and D.L. Feng, “Surface Electronic Structure and Isotropic Superconducting Gap in (Li<sub>0.8</sub>Fe<sub>0.2</sub>)OHFeSe”, *Phys. Rev. B* **92**, 060504(R) (2015).
- <sup>15</sup> Y.J. Yan, W.H. Zhang, M.Q. Ren, X. Liu, X.F. Lu, N. Z. Wang, X.H. Niu, Q. Fan, J. Miao, R. Tao, B.P. Xie, X.H. Chen, T. Zhang, D.L. Feng, “Surface Electronic Structure and Evidence of Plain S-Wave Superconductivity in (Li<sub>0.8</sub>Fe<sub>0.2</sub>)OHFeSe”, *Phys. Rev. B* **94**, 134502 (2016).
- <sup>16</sup> Y. Miyata, K. Nakayama, K. Suawara, T. Sato, and T. Takahashi, “High-Temperature Superconductivity in Potassium-Coated Multilayer FeSe Thin Films”, *Nat. Mater.* **14**, 775 (2015).
- <sup>17</sup> C.H.P. Wen, H.C. Xu, C. Chen, Z.C. Huang, X. Lou, Y.J. Pu, Q. Song, B.P. Xie, M. Abdel-Hafiez, D.A. Chareev, A.N. Vasiliev, R. Peng, and D.L. Feng, “Anomalous Correlation Effects and Unique Phase Diagram of Electron-Doped FeSe Revealed by Photoemission Spectroscopy”, *Nat. Comm.* **7**, 10840, (2016).

- <sup>18</sup> B. Lei, J.H. Cui, Z.J. Xiang, C. Shang, N.Z. Wang, G.J. Ye, X.G. Luo, T. Wu, Z. Sun, and X.H. Chen, “Evolution of High-Temperature Superconductivity from a Low- $T_c$  Phase Tuned by Carrier Concentration in FeSe Thin Flakes”, *Phys. Rev. Lett.* **116**, 077002 (2016).
- <sup>19</sup> K. Hanzawa, H. Sato, H. Hiramatsu, T. Kamiya, and H. Hosono, “Electric Field-Induced Superconducting Transition of Insulating FeSe Thin Film at 35 K”, *Proc. Nat. Acad. Sci.* **113**, 3986 (2016).
- <sup>20</sup> S.L. Bud’ko, M. Sturza, D.Y. Chung, M.G. Kanatzidis and P.C. Canfield, “Heat Capacity Jump at  $T_c$  and Pressure Derivatives of Superconducting Transition Temperature in the  $\text{Ba}_{1-x}\text{K}_x\text{Fe}_2\text{As}_2$  ( $0.2 \leq x \leq 1.0$ ) Series”, *Phys. Rev. B* **87**, 100509(R) (2013).
- <sup>21</sup> T. Sato, K. Nakayama, Y. Sekiba, P. Richard, Y.-M. Xu, S. Souma, T. Takahashi, G.F. Chen, J.L. Luo, N.L. Wang and H. Ding, “Band Structure and Fermi Surface of an Extremely Overdoped Iron-Based Superconductor  $\text{KFe}_2\text{As}_2$ ”, *Phys. Rev. Lett.* **103**, 047002 (2009).
- <sup>22</sup> T.A. Maier, S. Graser, P.J. Hirschfeld, D.J. Scalapino, “D-Wave Pairing from Spin Fluctuations in the  $\text{K}_x\text{Fe}_{2-y}\text{Se}_2$  Superconductors”, *Phys. Rev. B* **83**, 100515(R) (2011).
- <sup>23</sup> F. Wang, F. Yang, M. Gao, Z.-Y. Lu, T. Xiang, D.-H. Lee, “The Electron Pairing of  $\text{K}_x\text{Fe}_{2-y}\text{Se}_2$ ”, *Europhy. Lett.* **93**, 57003 (2011).
- <sup>24</sup> I.I. Mazin, “Symmetry Analysis of Possible Superconducting States in  $\text{K}_x\text{Fe}_y\text{Se}_2$  Superconductors”, *Phys. Rev. B* **84**, 024529 (2011).
- <sup>25</sup> P.A. Lee and X.-G. Wen, “Spin-Triplet P-Wave Pairing in a Three-Orbital Model for Iron Pnictide Superconductors”, *Phys. Rev. B* **78**, 144517 (2008).
- <sup>26</sup> V. Cvetkovic and O. Vafek, “Space Group Symmetry, Spin-Orbit Coupling, and the Low-Energy Effective Hamiltonian for Iron-Based Superconductors”, *Phys. Rev. B* **88**, 134510 (2013).
- <sup>27</sup> D.F. Agterberg, T. Shishidou, J. O’Halloran, P.M.R. Brydon, and M. Weinert, “Resilient Nodeless D-Wave Superconductivity in Monolayer FeSe”, *Phys. Rev. Lett.* **119**, 267001 (2017).
- <sup>28</sup> P.M. Eugenio and O. Vafek, “Classification of Symmetry Derived pairing at the M Point in FeSe”, *Phys. Rev. B* **98**, 014503 (2018).
- <sup>29</sup> M. Khodas and A.V. Chubukov, “Interpocket Pairing and Gap Symmetry in Fe-Based Superconductors with Only Electron Pockets”, *Phys. Rev. Lett.* **108**, 247003 (2012).
- <sup>30</sup> E. Berg, M.A. Metlitski and S. Sachdev, “Sign-Problem-Free Quantum Monte Carlo of the Onset of Antiferromagnetism in Metals”, *Science* **338**, 1606 (2012).
- <sup>31</sup> J.P. Rodriguez and R. Melendrez, “Fermi Surface Pockets in Electron-Doped Iron Superconductors”, *Phys. Rev. Lett.* **113**, 077001 (2014).

- tor by Lifshitz Transition”, J. Phys. Commun. **2**, 105011 (2018); “Corrigendum: Fermi Surface Pockets in Electron-Doped Iron Superconductor by Lifshitz Transition”, J. Phys. Commun. **3**, 019501 (2019).
- <sup>32</sup> C. Xu, M. Müller, and S. Sachdev, “Ising and Spin Orders in the Iron-Based Superconductors”, Phys. Rev. B **78**, 020501(R) (2008).
- <sup>33</sup> J. Kang and R.M. Fernandes, “Superconductivity in FeSe Thin Films Driven by the Interplay between Nematic Fluctuations and Spin-Orbit Coupling”, Phys. Rev. Lett. **117**, 217003 (2016).
- <sup>34</sup> J.P. Rodriguez, “Isotropic Cooper Pairs with Emergent Sign Changes in a Single-Layer Iron Superconductor”, Phys. Rev. B **95**, 134511 (2017).
- <sup>35</sup> S. Raghu, Xiao-Liang Qi, Chao-Xing Liu, D.J. Scalapino, Shou-Cheng Zhang, “Minimal Two-Band Model of the Superconducting Iron Oxypnictides”, Phys. Rev. B **77**, 220503(R) (2008).
- <sup>36</sup> J.P. Rodriguez, M.A.N. Araujo, P.D. Sacramento, “Emergent Nesting of the Fermi Surface from Local-Moment Description of Iron-Pnictide High- $T_c$  Superconductors”, Eur. Phys. J. B **87**, 163 (2014).
- <sup>37</sup> P.W. Anderson, “An Approximate Quantum Theory of the Antiferromagnetic Ground State”, Phys. Rev. **86**, 694 (1952).
- <sup>38</sup> B.I. Halperin and P.C. Hohenberg, “Hydrodynamic Theory of Spin Waves”, Phys. Rev. **188**, 898 (1969).
- <sup>39</sup> D. Forster, *Hydrodynamic Fluctuations, Broken Symmetry, and Correlation Functions* (Benjamin/Cummings), Reading, MA, 1975).
- <sup>40</sup> J.P. Rodriguez, “Magnetic Excitations in Ferropnictide Materials Controlled by a Quantum Critical Point into Hidden Order”, Phys. Rev. B **82**, 014505 (2010).
- <sup>41</sup> J.P. Rodriguez, “Spin Resonances in Iron-Selenide High- $T_c$  Superconductors by Proximity to Hidden Spin Density Wave”, Phys. Rev. B **102**, 024521 (2020).
- <sup>42</sup> G.M. Eliashberg, “Interactions between Electrons and Lattice Vibrations in a Superconductor”, Sov. Phys. JETP **11**, 696 (1960).
- <sup>43</sup> G.M. Eliashberg, “Temperature Green’s Function for Electrons in a Superconductor”, Sov. Phys. JETP **12**, 1000 (1961).
- <sup>44</sup> J.R. Schrieffer, *Theory of Superconductivity* (Benjamin, New York, 1964).
- <sup>45</sup> D.J. Scalapino, in *Superconductivity*, v. 1, ed. R.D. Parks (Dekker, New York, 1969).
- <sup>46</sup> Y. Nambu, “Quasi-Particles and Gauge Invariance in the Theory of Superconductivity”, Phys.

- Rev. **117**, 648 (1960).
- <sup>47</sup> L.P. Gorkov, Zh. Eksperim. i Teor. Fiz. **34**, 735 1958; “About the Energy Spectrum of Superconductors”, Sov. Phys. JETP **7**, 505 (1958).
- <sup>48</sup> I.I. Mazin, D.J. Singh, M.D. Johannes, and M.H. Du, “Unconventional Superconductivity with a Sign Reversal in the Order Parameter of  $\text{LaFeAsO}_{1-x}\text{F}_x$ ”, Phys. Rev. Lett. **101**, 057003 (2008).
- <sup>49</sup> K. Kuroki, S. Onari, R. Arita, H. Usui, Y. Tanaka, H. Kontani, and H. Aoki, “Unconventional Pairing Originating from the Disconnected Fermi Surfaces of Superconducting  $\text{LaFeAsO}_{1-x}\text{F}_x$ ”, Phys. Rev. Lett. **101**, 087004 (2008).
- <sup>50</sup> S. Graser, T.A. Maier, P.J. Hirschfeld, and D.J. Scalapino, “Near-Degeneracy of Several Pairing Channels in Multiorbital Models for the Fe Pnictides”, New J. Phys. **11**, 025016 (2009).
- <sup>51</sup> P. Morel and P.W. Anderson, “Calculation of the Superconducting State Parameters with Retarded Electron-Phonon Interaction”, Phys. Rev. **125**, 1263 (1962).
- <sup>52</sup> W.L. McMillan, “Transition Temperature of Strong-Coupled Superconductors”, Phys. Rev. **167**, 331 (1968).
- <sup>53</sup> *High-Temperature Superconductivity*, edited by V.L. Ginzburg and D.A. Kirzhnits (Consultants Bureau, New York, 1982).
- <sup>54</sup> J.P. Carbotte, “Properties of Boson-Exchange Superconductors”, Rev. Mod. Phys. **62**, 1027 (1990).
- <sup>55</sup> B. Pan, Y. Shen, D. Hu, Y. Feng, J.T. Park, A.D. Christianson, Q. Wang, Y. Hao, H. Wo, Z. Yin, T.A. Maier and J. Zhao, “Structure of Spin Excitations in Heavily Electron-Doped  $\text{Li}_{0.8}\text{Fe}_{0.2}\text{ODFeSe}$  Superconductors”, Nat. Comm. **8**, 123 (2017).
- <sup>56</sup> M. Yi, Z-K Liu, Y. Zhang, R. Yu, J.-X. Zhu, J.J. Lee, R.G. Moore, F.T. Schmitt, W. Li, S.C. Riggs, J.-H. Chu, B. Lv, J. Hu, M. Hashimoto, S.-K. Mo, Z. Hussain, Z.Q. Mao, C.W. Chu, I.R. Fisher, Q. Si, Z.-X. Shen, and D.H. Lu, “Observation of Universal Strong Orbital-Dependent Correlation Effects in Iron Chalcogenides”, Nat. Comm. **6**, 7777 (2015).
- <sup>57</sup> R. Yu and Q. Si, “Orbital-Selective Mott Phase in Multiorbital Models for Alkaline Iron Selenides  $\text{K}_{1-x}\text{Fe}_{2-y}\text{Se}_2$ ”, Phys. Rev. Lett. **110**, 146402 (2013).
- <sup>58</sup> See Supplemental Material: I. Add  $3d_{xy}$  Orbital to Eliashberg Theory with  $3d_{xz}/3d_{yz}$  Orbitals; II. Effects and Properties of  $3d_{xy}$  Orbital; III. Spin-Orbit Coupling.
- <sup>59</sup> O.V. Dolgov, I.I. Mazin, D. Parker, A.A. Golubov, “Interband Superconductivity: Contrasts between BCS and Eliashberg Theory”, Phys. Rev. **B79**, 060502(R) (2009); O.V. Dolgov, I.I.

- Mazin, D. Parker, A.A. Golubov, “Erratum: Interband Superconductivity: Contrasts between Bardeen-Cooper-Schrieffer and Eliashberg Theories [Phys. Rev. B 79, 060502(R) (2009)]”, Phys. Rev. B **80**, 219901(E) (2009).
- <sup>60</sup> L. Benfatto, E. Cappelluti, and C. Castellani, “Spectroscopic and Thermodynamic Properties in a Four-Band Model for Pnictides”, Phys. Rev. B **80**, 214522 (2009).
- <sup>61</sup> G. A. Ummarino, M. Tortello, D. Daghero, and R. S. Gonnelli “Three-Band  $s\pm$  Eliashberg Theory and the Superconducting Gaps of Iron Pnictides” Phys. Rev. B **80**, 172503 (2009).
- <sup>62</sup> M. Daghofer, A. Moreo, J.A. Riera, E. Arrigoni, D.J. Scalapino, and E. Dagotto, “Model for the Magnetic Order and Pairing Channels in Fe Pnictide Superconductors”, Phys. Rev. Lett. **101**, 237004 (2008); A. Moreo, M. Daghofer, J.A. Riera, and E. Dagotto, “Properties of a Two-Orbital Model for Oxypnictide Superconductors: Magnetic Order,  $B_{2g}$  Spin-Singlet Pairing Channel, and its Nodal Structure”, Phys. Rev. B **79**, 134502 (2009).

# Supplemental Material: Superconductivity by Hidden Spin Fluctuations in Electron-Doped Iron Selenide

Jose P. Rodriguez

*Department of Physics and Astronomy,  
California State University at Los Angeles, Los Angeles, CA 90032*

## I. ADD $3d_{xy}$ ORBITAL TO ELIASHBERG THEORY WITH $3d_{xz}/3d_{yz}$ ORBITALS

A Lifshitz transition from the unrenormalized Fermi surfaces displayed by Fig. 1 in the paper to the renormalized Fermi surfaces displayed by Fig. 4 in the paper is predicted by an Eliashberg Theory for electrons in the principal  $3d_{xz}/3d_{yz}$  orbitals interacting with hidden spin fluctuations at half filling. That analysis is found in section IV.A of the paper. Let us add a third  $3d_{xy}$  orbital. It then becomes important to recall that the heights of the selenium atoms above and below the square lattice of iron atoms make a checkerboard pattern. Lee and Wen pointed out<sup>S1</sup>, however, that an isolated layer of iron selenide is invariant under the glide-reflection symmetries  $T(a\hat{x})P_z$  and  $T(a\hat{y})P_z$ , where  $T(a\hat{x})$  and  $T(a\hat{y})$  are unit translations along the principal axes of the square lattice of iron atoms, and where  $P_z$  is a reflection about that square lattice. This symmetry permits the introduction of *pseudo momentum* quantum numbers,  $\tilde{\mathbf{k}}$ . Specifically, plane waves within the tight-binding approximation are given by

$$|\tilde{\mathbf{k}}, \alpha\rangle = N_{\text{Fe}}^{-1/2} \sum_{m,n} e^{i\tilde{\mathbf{k}} \cdot \mathbf{R}(m,n)} [T(a\hat{x})P_z]^m [T(a\hat{y})P_z]^n |\alpha\rangle, \quad (\text{S1})$$

where  $\mathbf{R}(m, n) = ma\hat{x} + na\hat{y}$  is an iron site, and where  $|\alpha\rangle$  is the boundstate for orbital  $\alpha$ . In the paper, and henceforth in this section and in the next one, all momentum quantum numbers  $\mathbf{k}$  coincide with pseudo momentum  $\tilde{\mathbf{k}}$ . Following Lee and Wen<sup>S1</sup>, assume an energy spectrum for the  $3d_{xy}$  electrons that disperses as

$$\varepsilon_{xy}(\mathbf{k}) = -2t_1^{xy}(\cos k_x a + \cos k_y a) - 2t_2^{xy}(\cos k_+ a + \cos k_- a), \quad (\text{S2})$$

where  $t_1^{xy}$  and  $t_2^{xy}$  are real nearest neighbor and next-nearest neighbor hopping matrix elements, and where  $k_{\pm} = k_x \pm k_y$ . Also assume that the  $3d_{xz}/3d_{yz}$  orbitals mix with the  $3d_{xy}$

orbital, with hopping matrix elements in momentum space of the form

$$\varepsilon_{xz,xy}(\mathbf{k}) = -2it_{xz,xy} \sin k_x a \quad \text{and} \quad \varepsilon_{yz,xy}(\mathbf{k}) = -2it_{yz,xy} \sin k_y a. \quad (\text{S3})$$

Here,  $t_{xz,xy}$  and  $t_{yz,xy}$  are real nearest neighbor hopping matrix elements that satisfy  $t_{xz,xy} = t_{yz,xy}$  by reflection symmetry. Last, assume a difference in energy of  $\Delta E$  between the  $3d_{xy}$  orbital and the degenerate  $3d_{xz}/3d_{yz}$  orbitals.

We shall now reconsider the analysis found in section IV.A of the paper of the Eliashberg Theory for electrons in  $3d_{xz}/3d_{yz}$  orbitals at half filling that interact with hidden spin fluctuations, but with the  $3d_{xy}$  orbital described above added to it. As in section IV.A of the paper, again assume that the superconducting gap is null at half filling. The electron propagator is then a  $3 \times 3$  matrix Greens function, with indices 1 for the anti-bonding ( $-$ ) band,  $d_{y(\delta)z}$ , 2 for the bonding ( $+$ ) band,  $d_{x(\delta)z}$ , and 3 for the  $d_{xy}$  band. In the absence of interactions, the matrix inverse of the bare electron propagator is then given by

$$G_0^{-1} = \begin{bmatrix} \omega - \varepsilon_- & 0 & -\varepsilon_{y(\delta)z,xy} \\ 0 & \omega - \varepsilon_+ & -\varepsilon_{x(\delta)z,xy} \\ -\varepsilon_{xy,y(\delta)z} & -\varepsilon_{xy,x(\delta)z} & \omega - \varepsilon_{xy} - \Delta E \end{bmatrix}. \quad (\text{S4})$$

Above, the off-diagonal Hamiltonian matrix elements are given by

$$\varepsilon_{x(\delta)z,xy} = (\cos \delta)\varepsilon_{xz,xy} - (\sin \delta)\varepsilon_{yz,xy} = \varepsilon_{xy,x(\delta)z}^*, \quad (\text{S5a})$$

$$\varepsilon_{y(\delta)z,xy} = (\sin \delta)\varepsilon_{xz,xy} + (\cos \delta)\varepsilon_{yz,xy} = \varepsilon_{xy,y(\delta)z}^*. \quad (\text{S5b})$$

Because hidden spin fluctuations interact exclusively with the degenerate  $3d_{xz}/3d_{yz}$  orbitals, self-energy corrections connected to the  $3d_{xy}$  orbital are null:  $\Sigma_{3,n} = 0 = \Sigma_{m,3}$ . Next, we shall henceforth confine ourselves to the regime of weak mixing between the  $3d_{xz}/3d_{yz}$  and  $3d_{xy}$  orbitals:  $\varepsilon_{y(\delta)z,xy}, \varepsilon_{x(\delta)z,xy} \rightarrow 0$ . We shall thereby neglect the contribution of such mixing to self-energy corrections among the  $n = 1$  and  $n = 2$  bands: e.g.,  $\Sigma_{1,2} \cong 0$ . Figure S1 displays the Feynman diagrams for the new Eliashberg equations within this approximation. The matrix inverse of the electron propagator within such an Eliashberg Theory therefore has the form

$$G^{-1} \cong \begin{bmatrix} Z\omega - (\varepsilon_- + \nu) & 0 & -\varepsilon_{y(\delta)z,xy} \\ 0 & Z\omega - (\varepsilon_+ - \nu) & -\varepsilon_{x(\delta)z,xy} \\ -\varepsilon_{xy,y(\delta)z} & -\varepsilon_{xy,x(\delta)z} & \omega - \varepsilon_{xy} - \Delta E \end{bmatrix}, \quad (\text{S6})$$

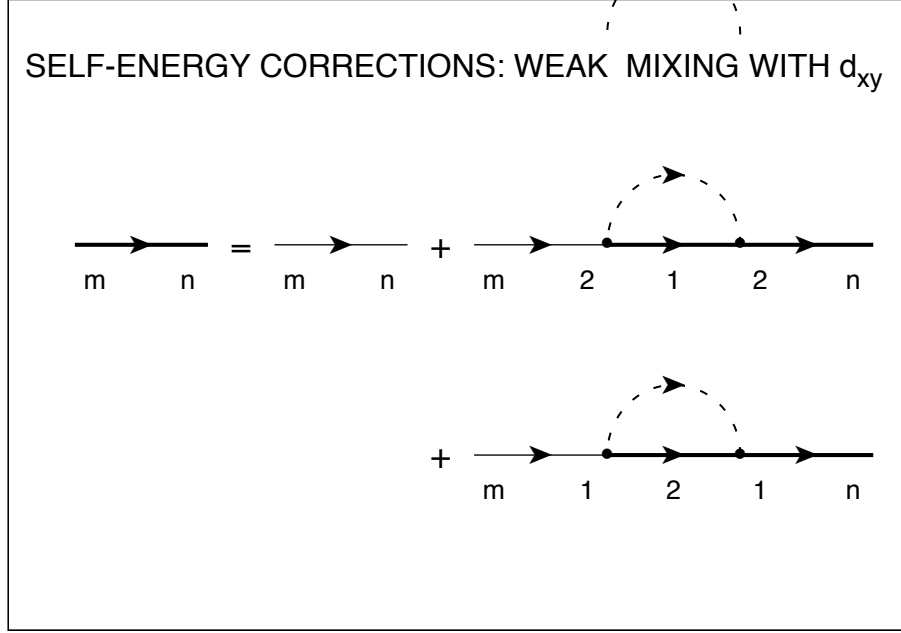


FIG. S1: Feynman diagrams for the original Eliashberg theory introduced in section III of the paper, but weakly coupled to the  $3d_{xy}$  band,  $n = 3$ . The band indices  $m$  and  $n$  run through 1, 2, and 3. See Eq. (S6) for the matrix inverse of the electron propagator.

where  $Z$  and  $\nu$  are the wavefunction renormalization and the band shift computed in section IV.A of the paper. Approaching quantum criticality,  $\Delta_b \rightarrow 0$ , and as the interaction with hidden spin fluctuations grows strong,  $U(\pi) \rightarrow \infty$ , recall that  $Z$  diverges at the Fermi level, while  $\nu$  approaches the upper band edge of  $\varepsilon_+(\mathbf{k})$ . Thus, a Lifshitz transition to the renormalized Fermi surfaces displayed by Fig. 4 in the paper is predicted.

The approximate 3-orbital Eliashberg theory encoded by the right-hand side of (S6) neglects contributions to the self-energy corrections of the  $3d_{xz}/3d_{yz}$  orbitals due to mixing with the  $3d_{xy}$  orbital. We can check the validity of this approximation by computing the Greens function via Cramer's Rule for the matrix inverse:

$$G_{i,j} = (-1)^{i-j} |g^{-1}(j, i)| / |G^{-1}|. \quad (\text{S7})$$

Above,  $g^{-1}(j, i)$  is the *minor*  $2 \times 2$  matrix at row  $j$  and column  $i$  of the matrix  $G^{-1}$ , while  $|G^{-1}|$  denotes the determinant of  $G^{-1}$ . In particular, for the diagonal component  $G_{1,1}$ , the

determinant of the minor matrix is

$$|g^{-1}(1, 1)| = [Z\omega - (\varepsilon_+ - \nu)](\omega - \varepsilon_{xy} - \Delta E) - |\varepsilon_{x(\delta)z,xy}|^2. \quad (\text{S8})$$

The determinant of  $G^{-1}$ , on the other hand, is

$$\begin{aligned} |G^{-1}| &= [Z\omega - (\varepsilon_- + \nu)][Z\omega - (\varepsilon_+ - \nu)](\omega - \varepsilon_{xy} - \Delta E) \\ &\quad - |\varepsilon_{y(\delta)z,xy}|^2[Z\omega - (\varepsilon_+ - \nu)] - |\varepsilon_{x(\delta)z,xy}|^2[Z\omega - (\varepsilon_- + \nu)]. \end{aligned} \quad (\text{S9})$$

Cramer's Rule (S7) then yields the result

$$G_{1,1} \cong \frac{1}{Z\omega - (\varepsilon_- + \nu)} + \frac{|\varepsilon_{y(\delta)z,xy}|^2}{[Z\omega - (\varepsilon_- + \nu)]^2(\omega - \varepsilon_{xy} - \Delta E)} \quad (\text{S10})$$

to lowest non-trivial order in the mixing with the  $3d_{xy}$  orbital. Similar calculations yield the result

$$G_{2,2} \cong \frac{1}{Z\omega - (\varepsilon_+ - \nu)} + \frac{|\varepsilon_{x(\delta)z,xy}|^2}{[Z\omega - (\varepsilon_+ - \nu)]^2(\omega - \varepsilon_{xy} - \Delta E)}. \quad (\text{S11})$$

Finally, the determinant of the minor matrix  $g^{-1}(2, 1)$  is  $|g^{-1}(2, 1)| = -\varepsilon_{y(\delta)z,xy}\varepsilon_{xy,x(\delta)z}$ .

Cramer's Rule (S7) then yields

$$G_{1,2} \cong \frac{\varepsilon_{y(\delta)z,xy}\varepsilon_{xy,x(\delta)z}}{[Z\omega - (\varepsilon_- + \nu)][Z\omega - (\varepsilon_+ - \nu)](\omega - \varepsilon_{xy} - \Delta E)} \quad (\text{S12})$$

to lowest order in the mixing with the  $3d_{xy}$  orbital. Last,  $G_{2,1} = G_{1,2}^*$ . By Fig. S2, we conclude that the contributions to the self-energy corrections among the  $3d_{xz}/3d_{yz}$  orbitals due to the  $3d_{xy}$  orbital are second order in the mixing. By comparison with (S6), they can therefore be neglected in the regime of weak mixing with the  $3d_{xy}$  orbital. This confirms the previous assumption that  $\Sigma_{1,2} \cong 0$ .

## II. EFFECTS AND PROPERTIES OF $3d_{xy}$ ORBITAL

The form of the inverse Greens function (S6) implies level repulsion of the degenerate  $3d_{xz}/3d_{yz}$  bands because of mixing with the  $3d_{xy}$  band. In particular, the Fermi surfaces are determined by the characteristic equation  $|G^{-1}(\omega)| = 0$ . Directly expanding the latter (S9) yields the third-order polynomial in frequency

$$|G^{-1}| = a_3\omega^3 + a_2\omega^2 + a_1\omega + a_0, \quad (\text{S1})$$

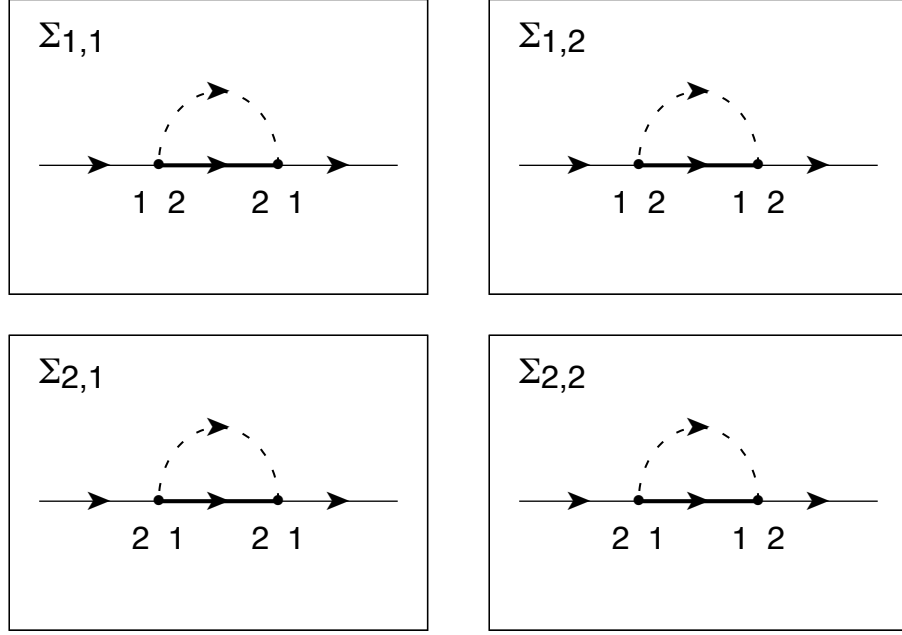


FIG. S2: All possible self-energy corrections due to interactions with hidden spin fluctuations in the presence of mixing between the  $3d_{xz}/3d_{yz}$  bands, 1 and 2, and the  $3d_{xy}$  band, 3.

with coefficients

$$a_3 = Z^2, \quad (\text{S2a})$$

$$a_2 = -(\varepsilon_{xy} + \Delta E)Z^2 - (\varepsilon_+ + \varepsilon_-)Z, \quad (\text{S2b})$$

$$a_1 = (\varepsilon_{xy} + \Delta E)(\varepsilon_+ + \varepsilon_-)Z - (|\varepsilon_{y(\delta)z,xy}|^2 + |\varepsilon_{x(\delta)z,xy}|^2)Z + (\varepsilon_- + \nu)(\varepsilon_+ - \nu), \quad (\text{S2c})$$

$$a_0 = -(\varepsilon_- + \nu)(\varepsilon_+ - \nu)(\varepsilon_{xy} + \Delta E) + (\varepsilon_+ - \nu)|\varepsilon_{y(\delta)z,xy}|^2 + (\varepsilon_- + \nu)|\varepsilon_{x(\delta)z,xy}|^2. \quad (\text{S2d})$$

Above, the magnitude squared of the mixing matrix elements are given explicitly by

$$|\varepsilon_{x(\delta)z,xy}|^2 = \frac{1}{2}(1 + \cos 2\delta)|\varepsilon_{xz,xy}|^2 - (\sin 2\delta)|\varepsilon_{xz,xy}\varepsilon_{yz,xy}| + \frac{1}{2}(1 - \cos 2\delta)|\varepsilon_{yz,xy}|^2, \quad (\text{S3a})$$

$$|\varepsilon_{y(\delta)z,xy}|^2 = \frac{1}{2}(1 - \cos 2\delta)|\varepsilon_{xz,xy}|^2 + (\sin 2\delta)|\varepsilon_{xz,xy}\varepsilon_{yz,xy}| + \frac{1}{2}(1 + \cos 2\delta)|\varepsilon_{yz,xy}|^2, \quad (\text{S3b})$$

with  $\cos 2\delta$  and  $\sin 2\delta$  given by expressions (6a) and (6b) in the paper. Notice, as expected, that

$$|\varepsilon_{x(\delta)z,xy}|^2 + |\varepsilon_{y(\delta)z,xy}|^2 = |\varepsilon_{xz,xy}|^2 + |\varepsilon_{yz,xy}|^2.$$

Figure S3b displays the resulting Fermi surfaces, with hopping matrix elements among the  $3d_{xz}/3d_{yz}$  orbitals that are identical to those in Fig. 4 of the paper for the renormalized band structure:  $t_1^{\parallel} = 100$  meV,  $t_1^{\perp} = 500$  meV,  $t_2^{\parallel} = 0$ , and  $t_2^{\perp}/i = 100$  meV. The energy shift between the two  $3d_{xz}/3d_{yz}$  bands is set by the staggered chemical potential  $\nu = 1.7$  eV. A relatively flat hole-type dispersion for the  $3d_{xy}$  band is taken<sup>S1</sup>, with hopping matrix elements  $t_1^{xy} = -40$  meV and  $t_2^{xy} = -28$  meV, along with  $3d_{xz}/3d_{yz}$ - $3d_{xy}$  mixing  $t_1^{xz,xy} = 20$  meV =  $t_1^{yz,xy}$ . Last, the energy splitting between the  $3d_{xy}$  and  $3d_{xz}/3d_{yz}$  orbitals is tuned to  $\Delta E = 20$  meV, at which point the system of three bands is half filled. Figure S3a shows the corresponding Fermi surfaces in the absence of mixing with the  $3d_{xy}$  band:  $t_1^{xz,xy} = 0 = t_1^{yz,xy}$ . The system of three bands is slightly electron doped in such case. Comparison of Figs. S3a and S3b reveals the expected level repulsion of electron/hole Fermi surface pockets because of mixing with the  $3d_{xy}$  band. At half filling, the renormalized bands  $\varepsilon_-(\mathbf{k}) + \nu$  and  $\varepsilon_+(\mathbf{k}) - \nu$  inter-penetrate at energies near the Fermi level, forming hybridized energy dispersions similar in shape to the *universal joint* in a drive shaft.

And what is the effect of the wavefunction renormalization  $Z$  of the  $3d_{xz}/3d_{yz}$  bands on the  $3d_{xy}$  band? To answer this question, let us first write the determinant of the matrix inverse (S6) as  $|G^{-1}(\omega)| = Z^2(\omega - \omega_1)(\omega - \omega_2)(\omega - \omega_3)$ , where  $\omega_1$ ,  $\omega_2$ , and  $\omega_3$  are the three roots of the characteristic equation  $|G^{-1}(\omega)| = 0$ . Near the Fermi surface of the  $3d_{xy}$  band shown by Fig. S3b,  $\omega_3(\mathbf{k}) = 0$ , the former determinant can therefore be approximated by  $|G^{-1}(\omega)| = A_3(\omega - \omega_3)$ , with a constant prefactor

$$A_3 = \frac{\partial}{\partial \omega} |G^{-1}|_3 = 3a_3\omega_3^2 + 2a_2\omega_3 + a_1 = a_1. \quad (\text{S4})$$

Yet the determinant of the  $2 \times 2$  minor matrix  $g^{-1}(3, 3)$  of (S6) is

$$|g^{-1}(3, 3)| = [Z\omega - (\varepsilon_- + \nu)][Z\omega - (\varepsilon_+ - \nu)]. \quad (\text{S5})$$

Cramer's Rule (S7) thereby yields the following diagonal component for the electron propagator in the  $3d_{xy}$  band near the Fermi surface,  $\omega_3(\mathbf{k}) = 0$ :

$$G_{3,3}(\omega) = \frac{Z_3^{-1}}{\omega - \omega_3} \quad \text{with} \quad Z_3 = \frac{a_1}{(\varepsilon_- + \nu)(\varepsilon_+ - \nu)}. \quad (\text{S6})$$

Last, the characteristic equation at the Fermi surface is equivalent to  $a_0 = 0$ . Study of the expression (S2d) for the coefficient  $a_0$  yields the identity

$$\varepsilon_{xy} + \Delta E = \frac{|\varepsilon_{y(\delta)z,xy}|^2}{\varepsilon_- + \nu} + \frac{|\varepsilon_{x(\delta)z,xy}|^2}{\varepsilon_+ - \nu}. \quad (\text{S7})$$

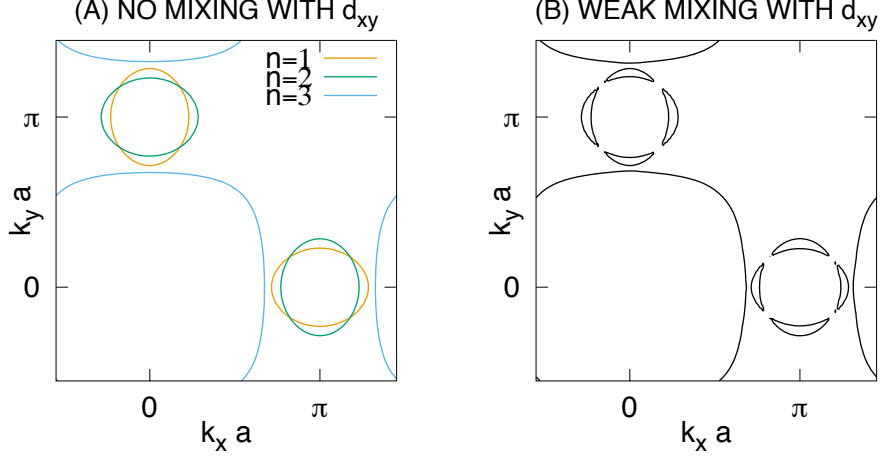


FIG. S3: Fermi surfaces of  $3d_{xz}/3d_{yz}$  bands ( $n = 1, 2$ ) weakly mixing with the  $3d_{xy}$  band ( $n = 3$ ). The  $3d_{xz}/3d_{yz}$  bands are identical to Fig. 4 in the paper, while the  $3d_{xy}$  band is hole-type and relatively flat, with nearest neighbor and next-nearest neighbor hopping parameters  $t_1^{xy} = -40$  meV and  $t_2^{xy} = -28$  meV. The splitting between the  $3d_{xy}$  and the  $3d_{xz}/3d_{yz}$  orbitals is set to  $\Delta E = 20$  meV. As in the paper, the momentum  $(k_x, k_y)$  coincides with *pseudo momentum*. (See ref.<sup>S1</sup> and the text.)

After substituting it into the expression (S2c) for the coefficient  $a_1$ , (S6) then ultimately yields the following result for the inherited wavefunction renormalization:

$$Z_3 = 1 + \left[ \frac{|\varepsilon_y(\delta)z,xy|^2}{(\varepsilon_- + \nu)^2} + \frac{|\varepsilon_x(\delta)z,xy|^2}{(\varepsilon_+ - \nu)^2} \right] Z. \quad (\text{S8})$$

The  $3d_{xy}$  band therefore inherits the divergent wavefunction renormalization of the  $3d_{xz}/3d_{yz}$  bands at the Fermi level,  $\omega \rightarrow 0$ :  $Z \rightarrow \infty$  implies  $Z_3 \rightarrow \infty$ .

And how do the above results depend on changes in the nature of the three Fermi surfaces in the absence of mixing with the  $3d_{xy}$  orbital that are shown in Fig. S3a ? Increasing the size of the hole-type Fermi surface ( $n = 3$ ) for the  $3d_{xy}$  electrons is achieved by increasing the energy splitting  $\Delta E$  between the  $3d_{xy}$  and  $3d_{xz}/3d_{yz}$  orbitals, while increasing the size

$\langle m H_{\text{SO}} n\rangle$	$ d_{y(\delta)z}, \uparrow\rangle$	$ d_{x(\delta)z}, \uparrow\rangle$	$ d_{xy}, \downarrow\rangle$
$\langle d_{y(\delta)z}, \uparrow  $	0	$+i\lambda_{\text{SO}}/2$	$-e^{-i\delta}\lambda_{\text{SO}}/2$
$\langle d_{x(\delta)z}, \uparrow  $	$-i\lambda_{\text{SO}}/2$	0	$+ie^{-i\delta}\lambda_{\text{SO}}/2$
$\langle d_{xy}, \downarrow  $	$-e^{+i\delta}\lambda_{\text{SO}}/2$	$-ie^{+i\delta}\lambda_{\text{SO}}/2$	0

TABLE I: Matrix elements for spin-orbit coupling, Eq. (S1), in the “up” irreducible Hilbert space. See Eq. (S2).

of the electron/hole Fermi surface pockets ( $n = 1, 2$ ) for the  $3d_{xz}/3d_{yz}$  electrons is achieved by lowering the on-site repulsive energy  $U(\pi)$ . [See Eq. (42) in the paper.] Either of these changes in parameters can result in  $3d_{xy}$  orbital character at the tips of the electron Fermi surface pockets,  $n = 1$ . (Cf. Fig. S3a.) It coincides with predictions made by band-structure calculations in the case of alkali-metal intercalated iron selenides<sup>S2,S3</sup>.

### III. SPIN-ORBIT COUPLING

Consider next adding spin-orbit coupling at each iron atom:

$$H_{\text{SO}} = \lambda_{\text{SO}}\mathbf{L} \cdot \mathbf{S} = \lambda_{\text{SO}}\left(\frac{1}{2}L_+S_- + \frac{1}{2}L_-S_+ + L_zS_z\right). \quad (\text{S1})$$

The principal iron orbitals at the electron Fermi surface pockets in FeSe are the degenerate  $3d_{xz}/3d_{yz}$  orbitals and the  $3d_{xy}$  orbital. Henceforth, we therefore shall project out the  $3d_{x^2-y^2}$  and the  $3d_{2z^2-x^2-y^2}$  orbitals<sup>S4-S6</sup>. Two irreducible Hilbert spaces thereby emerge under the spin-orbit Hamiltonian (S1):

$$\{|d_{y(\delta)z}, \uparrow\rangle, |d_{x(\delta)z}, \uparrow\rangle, |d_{xy}, \downarrow\rangle\} \quad \text{and} \quad \{|d_{y(\delta)z}, \downarrow\rangle, |d_{x(\delta)z}, \downarrow\rangle, |d_{xy}, \uparrow\rangle\}. \quad (\text{S2})$$

Above,  $x(\delta)$  and  $y(\delta)$  are the orbital coordinates measured with respect to new axes rotated by an angle  $-\delta$  about the  $z$  axis. Matrix elements of  $H_{\text{SO}}$  between the two Hilbert spaces above are null. On the other hand, matrix elements of  $H_{\text{SO}}$  within each one the two Hilbert spaces above are easily computed, and these are listed in Tables I and II.

In the previous sections, all momentum quantum numbers  $\mathbf{k}$  coincide with pseudo momentum<sup>S1</sup>  $\tilde{\mathbf{k}}$ . Specifically, plane waves within the tight-binding approximation have the form (S1). Yet does pseudo momentum remain a good quantum number when the spin-orbit interaction (S1) at each iron atom is included? Observe that  $P_z^{-1}L_xP_z = -L_x$ , that

$\langle m H_{\text{SO}} n\rangle$	$ d_{y(\delta)z}, \downarrow\rangle$	$ d_{x(\delta)z}, \downarrow\rangle$	$ d_{xy}, \uparrow\rangle$
$\langle d_{y(\delta)z}, \downarrow  $	0	$-i\lambda_{\text{SO}}/2$	$+e^{+i\delta}\lambda_{\text{SO}}/2$
$\langle d_{x(\delta)z}, \downarrow  $	$+i\lambda_{\text{SO}}/2$	0	$+ie^{+i\delta}\lambda_{\text{SO}}/2$
$\langle d_{xy}, \uparrow  $	$+e^{-i\delta}\lambda_{\text{SO}}/2$	$-ie^{-i\delta}\lambda_{\text{SO}}/2$	0

TABLE II: Matrix elements for spin-orbit coupling, Eq. (S1), in the “down” irreducible Hilbert space. See Eq. (S2).

$P_z^{-1}L_yP_z = -L_y$ , and that  $P_z^{-1}L_zP_z = +L_z$ . Angular momentum then does not commute with a reflection about the  $x$ - $y$  plane, hence pseudo momentum is no longer a good quantum number when the spin-orbit interaction (S1) is included.

The square lattice of spin-orbit interactions (S1) does, however, commute with  $T(a\hat{x})$  and with  $T(a\hat{y})$ . This means that conventional crystal momentum  $\mathbf{k}$  remains a good quantum number, with conventional tight-binding plane waves

$$|\mathbf{k}, \alpha\rangle = N_{\text{Fe}}^{-1/2} \sum_{m,n} e^{i\mathbf{k}\cdot\mathbf{R}(m,n)} [T(a\hat{x})]^m [T(a\hat{y})]^n |\alpha\rangle. \quad (\text{S3})$$

If we turn off the contribution due to electrostatic interactions to hopping between the  $3d_{xz}/3d_{yz}$  orbitals and the  $3d_{xy}$  orbital,  $t_{xz,xy} = 0 = t_{yz,xy}$ , then the on-site irreducible Hilbert spaces (S2) under the spin-orbit interaction can be extended to the following sets of plane-wave states:

$$\{|\mathbf{k}, d_{y(\delta)z}, \uparrow\rangle, |\mathbf{k}, d_{x(\delta)z}, \uparrow\rangle, |\mathbf{k}, d_{xy}, \downarrow\rangle\} \quad \text{and} \quad \{|\mathbf{k}, d_{y(\delta)z}, \downarrow\rangle, |\mathbf{k}, d_{x(\delta)z}, \downarrow\rangle, |\mathbf{k}, d_{xy}, \uparrow\rangle\}. \quad (\text{S4})$$

Observe, now, that  $P_z|d_{x(\delta)z}\rangle = -|d_{x(\delta)z}\rangle$  and  $P_z|d_{y(\delta)z}\rangle = -|d_{y(\delta)z}\rangle$ , while  $P_z|d_{xy}\rangle = +|d_{xy}\rangle$ . By (S1), this means that the conventional crystal momentum for electrons in the  $3d_{xz}/3d_{yz}$  orbitals is shifted with respect to the pseudo momentum by the checkerboard wavenumber  $\mathbf{Q}_{\text{AF}}$ , while that the conventional crystal momentum for electrons in the  $3d_{xy}$  orbital coincides with the pseudo momentum. In conclusion, the inverse Greens function for the Eliashberg Theory in the paper, at null superconducting gaps, has the form

$$G^{-1} \cong \begin{bmatrix} Z\omega - (\varepsilon_- + \nu) & -\varepsilon_{y(\delta)z,x(\delta)z} & -\varepsilon_{y(\delta)z,xy} \\ -\varepsilon_{x(\delta)z,y(\delta)z} & Z\omega - (\varepsilon_+ - \nu) & -\varepsilon_{x(\delta)z,xy} \\ -\varepsilon_{xy,y(\delta)z} & -\varepsilon_{xy,x(\delta)z} & \omega - \bar{\varepsilon}_{xy} - \Delta E \end{bmatrix}, \quad (\text{S5})$$

where  $\bar{\varepsilon}_{xy}(\mathbf{k}) = \varepsilon_{xy}(\mathbf{k} + \mathbf{Q}_{AF})$ , and where the off-diagonal matrix elements above,  $\varepsilon_{\alpha,\beta}$ , coincide with those for the spin-orbit interaction that are listed in Tables I and II.

The determinant of the inverse Greens function (S5) is given by

$$\begin{aligned}
|G^{-1}| &= [Z\omega - (\varepsilon_- + \nu)][Z\omega - (\varepsilon_+ - \nu)](\omega - \bar{\varepsilon}_{xy} - \Delta E) \\
&\quad - |\varepsilon_{y(\delta)z,xy}|^2 [Z\omega - (\varepsilon_+ - \nu)] - |\varepsilon_{x(\delta)z,xy}|^2 [Z\omega - (\varepsilon_- + \nu)] \\
&\quad - |\varepsilon_{y(\delta)z,x(\delta)z}|^2 (\omega - \bar{\varepsilon}_{xy} - \Delta E) \\
&\quad - \varepsilon_{y(\delta)z,x(\delta)z} \varepsilon_{x(\delta)z,xy} \varepsilon_{xy,y(\delta)z} - \varepsilon_{x(\delta)z,y(\delta)z} \varepsilon_{y(\delta)z,xy} \varepsilon_{xy,x(\delta)z}.
\end{aligned} \tag{S6}$$

Then by Cramer's Rule (S7), the Greens functions among the  $3d_{xz}/3d_{yz}$  orbitals are given by diagonal components  $G_{1,1} \cong [Z\omega - (\varepsilon_- + \nu)]^{-1}$  and  $G_{2,2} \cong [Z\omega - (\varepsilon_+ - \nu)]^{-1}$ , and by off-diagonal components  $G_{1,2} \cong \varepsilon_{y(\delta)z,x(\delta)z} / ([Z\omega - (\varepsilon_- + \nu)][Z\omega - (\varepsilon_+ - \nu)])$  and  $G_{2,1} = G_{1,2}^*$ , up to first order in the spin-orbit coupling,  $\lambda_{SO}$ . Substituting the latter into the off-diagonal self-energy corrections depicted by Fig. S2 yields that the portion of the spin-orbit interaction,  $\lambda_{SO}L_zS_z$ , that is represented by the off-diagonal matrix elements  $\varepsilon_{x(\delta)z,y(\delta)z}$  and  $\varepsilon_{y(\delta)z,x(\delta)z}$  receives substantial renormalization within Eliashberg Theory. On the other hand, substitution of the former into Fig. S2 suggests that the divergent wave function renormalization and the Lifshitz transition that are predicted in the absence of the  $3d_{xy}$  orbital by Eliashberg Theory survive the addition of the  $3d_{xy}$  orbital and of the spin-orbit interaction.

And as in the previous case of the background electrostatic potential, do the electrons at the Fermi surface of the  $3d_{xy}$  band,  $\omega_3(\mathbf{k})$ , inherit the infinite wavefunction renormalization from the  $3d_{xz}/3d_{yz}$  bands at the Fermi surface at half filling? To answer this question, we first expand the expression above for the determinant (S6). This yields the third-order polynomial (S1), with coefficients that are given by

$$a_3 = Z^2, \tag{S7a}$$

$$a_2 = -(\bar{\varepsilon}_{xy} + \Delta E)Z^2 - (\varepsilon_+ + \varepsilon_-)Z, \tag{S7b}$$

$$\begin{aligned}
a_1 &= (\bar{\varepsilon}_{xy} + \Delta E)(\varepsilon_+ + \varepsilon_-)Z - (|\varepsilon_{y(\delta)z,xy}|^2 + |\varepsilon_{x(\delta)z,xy}|^2)Z \\
&\quad - |\varepsilon_{y(\delta)z,x(\delta)z}|^2 + (\varepsilon_- + \nu)(\varepsilon_+ - \nu),
\end{aligned} \tag{S7c}$$

$$\begin{aligned}
a_0 &= -(\varepsilon_- + \nu)(\varepsilon_+ - \nu)(\bar{\varepsilon}_{xy} + \Delta E) + (\varepsilon_+ - \nu)|\varepsilon_{y(\delta)z,xy}|^2 + (\varepsilon_- + \nu)|\varepsilon_{x(\delta)z,xy}|^2 \\
&\quad + (\bar{\varepsilon}_{xy} + \Delta E)|\varepsilon_{y(\delta)z,x(\delta)z}|^2 - \varepsilon_{y(\delta)z,x(\delta)z} \varepsilon_{x(\delta)z,xy} \varepsilon_{xy,y(\delta)z} - \varepsilon_{x(\delta)z,y(\delta)z} \varepsilon_{y(\delta)z,xy} \varepsilon_{xy,x(\delta)z}.
\end{aligned} \tag{S7d}$$

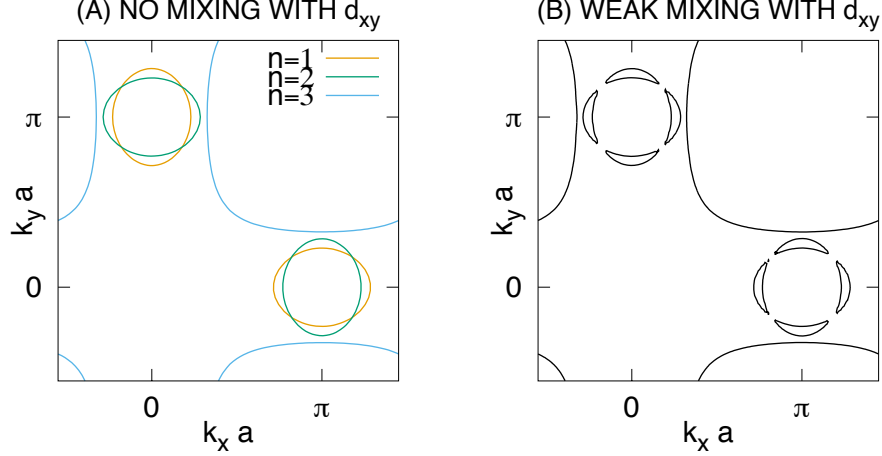


FIG. S4: Fermi surfaces of  $3d_{xz}/3d_{yz}$  bands ( $n = 1, 2$ ) weakly mixing with the  $3d_{xy}$  band ( $n = 3$ ) via the spin-orbit interactions at each iron atom. The  $3d_{xz}/3d_{yz}$  bands are identical to those in Fig. 4 of the paper. Also, the  $3d_{xy}$  band is identical to that in Fig. S3, but the momentum  $(k_x, k_y)$  coincides with the crystal momentum shifted by the checkerboard wavevector  $(\pi/a, \pi/a)$ .

The off-diagonal matrix elements above,  $\varepsilon_{\alpha,\beta}$ , are listed in Tables I and II. Following the previous analysis (S4), the determinant at frequencies  $\omega$  approaching the Fermi surface,  $\omega_3(\mathbf{k}) = 0$ , is given by  $|G^{-1}(\omega)| = a_1(\omega - \omega_3)$ . And in the present case, the  $2 \times 2$  minor matrix  $g^{-1}(3, 3)$  has determinant

$$|g^{-1}(3, 3)| = [Z\omega - (\varepsilon_- + \nu)][Z\omega - (\varepsilon_+ - \nu)] - |\varepsilon_{y(\delta)z, x(\delta)z}|^2. \quad (\text{S8})$$

By Cramer's Rule (S7), the wavefunction renormalization at the Fermi surface for  $3d_{xy}$  electrons is then

$$Z_3 = \frac{a_1}{(\varepsilon_- + \nu)(\varepsilon_+ - \nu) - |\varepsilon_{y(\delta)z, x(\delta)z}|^2}. \quad (\text{S9})$$

Now recall that the Fermi surface is determined by the characteristic equation  $a_0 = 0$ . Using expression (S7d) for the coefficient  $a_0$  thereby yields the identity (S7) to lowest non-trivial

order in the mixing with the  $3d_{xy}$  orbital, with the exception that  $\varepsilon_{xy}$  is replaced by  $\bar{\varepsilon}_{xy}$ . After substituting it into expression (S7c) for the coefficient  $a_1$ , (S9) in turn yields expression (S8) for the wavefunction renormalization at weak mixing with the  $3d_{xy}$  orbital, in the regime of large wavefunction renormalization,  $Z \gg 1$ . The wavefunction renormalization  $Z_3^{-1}$  is therefore positive, and it vanishes as  $Z \rightarrow \infty$ .

Figure S4b shows the Fermi surfaces set by the characteristic equation  $|G^{-1}| = 0$  at  $\omega = 0$ ; i.e.,  $a_0(\mathbf{k}) = 0$ . The  $3d_{xz}/3d_{yz}$  and  $3d_{xy}$  bands in isolation are identical to those shown by Fig. S3a, but the momentum  $(k_x, k_y)$  instead coincides with the crystal momentum shifted by the checkerboard wavevector  $(\pi/a, \pi/a)$ . Here, the spin-orbit coupling energy is set to  $\lambda_{\text{SO}} = 14$  meV. Notice the expected level repulsion shown by the  $3d_{xz}/3d_{yz}$  Fermi surface pockets at  $(\pi/a, 0)$  and  $(0, \pi/a)$  in Fig. S4b. The electronic filling fraction is close to half filling.

- 
- [S1] P.A. Lee and X.-G. Wen, “Spin-Triplet P-Wave Pairing in a Three-Orbital Model for Iron Pnictide Superconductors”, *Phys. Rev. B* **78**, 144517 (2008).
- [S2] T.A. Maier, S. Graser, P.J. Hirschfeld, D.J. Scalapino, “D-Wave Pairing from Spin Fluctuations in the  $\text{K}_x\text{Fe}_{2-y}\text{Se}_2$  Superconductors”, *Phys. Rev. B* **83**, 100515(R) (2011).
- [S3] I.I. Mazin, “Symmetry Analysis of Possible Superconducting States in  $\text{K}_x\text{Fe}_y\text{Se}_2$  Superconductors”, *Phys. Rev. B* **84**, 024529 (2011).
- [S4] V. Cvetkovic and O. Vafek, “Space Group Symmetry, Spin-Orbit Coupling, and the Low-Energy Effective Hamiltonian for Iron-Based Superconductors”, *Phys. Rev. B* **88**, 134510 (2013).
- [S5] D.F. Agterberg, T. Shishidou, J. O’Halloran, P.M.R. Brydon, and M. Weinert, “Resilient Nodeless D-Wave Superconductivity in Monolayer FeSe”, *Phys. Rev. Lett.* **119**, 267001 (2017).
- [S6] P.M. Eugenio and O. Vafek, “Classification of Symmetry Derived pairing at the M Point in FeSe”, *Phys. Rev. B* **98**, 014503 (2018).